

1 **The Dynamics of Unlikely Slip: 3D Modeling of Low-angle Normal Fault Rupture at**
2 **the Mai'iu Fault, Papua New Guinea**
3

4 **J. Biemiller¹, A.-A. Gabriel^{1,2}, and T. Ulrich²**

5 ¹ Institute of Geophysics and Planetary Physics, Scripps Institution of Oceanography, University
6 of California San Diego, La Jolla, California, USA.

7 ² Department of Earth and Environmental Sciences, Ludwig Maximilian University of Munich,
8 Munich, Germany.

9
10 Corresponding author: James Biemiller (jbiemiller@ucsd.edu)

11 **Key Points:**

- 12 • We perform the first 3D dynamic rupture simulations of low-angle normal fault
13 earthquake scenarios constrained by laboratory & field evidence
- 14 • Large low-angle normal fault earthquakes are dynamically viable under various stress
15 conditions including perfectly Andersonian extension
- 16 • Shallow slip is limited by the stabilizing effects of shallow fault geometry, velocity-
17 strengthening gouges, and free-surface interactions
18

19 Abstract

20 Despite decades-long debate over the mechanics of low-angle normal faults dipping less
21 than 30°, many questions about their strength, stress, and slip remain unresolved. Recent
22 geologic and geophysical observations have confirmed that gently-dipping detachment faults can
23 slip at such shallow dips and host moderate-to-large earthquakes. Here, we analyze the first 3D
24 dynamic rupture models to assess how different stress and strength conditions affect rupture
25 characteristics of low-angle normal fault earthquakes. We model observationally constrained
26 spontaneous rupture under different loading conditions on the active Mai'iu fault in Papua New
27 Guinea, which dips 16-24° at the surface and accommodates ~8 mm/yr of horizontal extension.
28 We analyze four distinct fault-local stress scenarios: 1) Andersonian extension, as inferred in the
29 hanging wall; 2) back-rotated principal stresses inferred paleopiezometrically from the exhumed
30 footwall; 3) favorably rotated principal stresses well-aligned for low-angle normal-sense slip;
31 and 4) Andersonian extension derived from depth-variable static fault friction decreasing
32 towards the surface. Our modeling suggests that subcritically stressed detachment faults can host
33 moderate earthquakes within purely Andersonian stress fields. Near-surface rupture is impeded
34 by free-surface stress interactions and dynamic effects of the gently-dipping geometry and
35 frictionally stable gouges of the shallowest portion of the fault. Although favorably-inclined
36 principal stresses have been proposed for some detachments, these conditions are not necessary
37 for seismic slip on these faults. Our results demonstrate how integrated geophysical and geologic
38 observations can constrain dynamic rupture model parameters to develop realistic rupture
39 scenarios of active faults that may pose significant seismic and tsunami hazards to nearby
40 communities.

41 Plain Language Summary

42 Movement across faults allow parts of the Earth's crust to move past each other in
43 response to forces driven by tectonic plate motions and can occur during large, devastating
44 earthquakes. The orientation of a fault relative to the direction of the forces and stresses loading
45 determines how easily it can 'slip' in any given direction and whether it will continue to slip or if
46 new fractures and faults will form instead. Some faults appear to be geometrically misoriented
47 and thus 'locked' relative to their local forces, but nonetheless continue to move on the scale of
48 mm per year and accommodate crustal motions. Here, we develop data-constrained computer
49 models to test how different forces at depth affect the movement and associated potential
50 earthquake magnitude of one of these misoriented faults: the Mai'iu normal fault in Papua New
51 Guinea. Our results suggest these faults can indeed slip in large earthquakes under tectonic
52 crustal stress conditions, and that locally favorably rotated stresses would generate even larger
53 earthquakes. We find that seismic slip does not always reach the Earth's surface and explore
54 various physical mechanisms limiting near-surface slip on these faults.

55 **1 Introduction**

56 1.1 Active Low Angle Normal Faults

57 Normal-sense slip on shallowly-dipping ($<30^\circ$) detachment faults has helped
58 accommodate tens of kilometers of geologically recorded localized extension in a variety of rift
59 settings (e.g., Collettini et al., 2011). The mechanics of these low-angle normal faults (LANFs)
60 have been extensively debated because such shallowly dipping normal faults appear to defy
61 classic fault mechanical theory. Anderson-Byerlee frictional fault reactivation theory predicts
62 that extension of crustal rocks with Byerlee friction ($0.6 \leq$ static friction coefficient, $\mu_s \leq 0.85$) in
63 an Andersonian stress field (characterized by one vertical principal stress direction) should form
64 normal faults dipping $60\text{-}75^\circ$ and that these faults should frictionally lock up and stop slipping if
65 rotated to dips less than 30° (e.g., Sibson, 1990).

66 Despite the global abundance of LANFs, the 2010 M_w 7.2 El Mayor-Cucapah earthquake
67 in Mexico was potentially the first instrumentally recorded $M_w > 7$ earthquake to involve
68 coseismic rupture of a LANF (Fletcher et al., 2014, 2016). Understanding the seismogenic
69 potential of LANFs has been complicated by the scarcity of active LANFs and the paucity of
70 instrumentally recorded large ($M_w > 7$) normal-sense earthquakes with well-resolved shallowly-
71 dipping focal mechanisms (Jackson & White, 1989; Collettini & Sibson, 2001; Collettini, 2011);
72 however, active LANFs slipping up to 1 cm/yr are now well-documented (Webber et al., 2018).
73 Moreover, recent neotectonic (Hayman et al., 2003; Numelin et al., 2007a; Little et al., 2019;
74 Cummins et al., 2020; Biemiller et al., 2020a), seismological (Abers et al., 1997; Abers, 2001;
75 Fletcher et al., 2014, 2016), and geodetic (Anderlini et al., 2016; Biemiller et al., 2020b)
76 evidence from both ancient and active LANFs suggest that these fault systems can host
77 moderate-to-large $M_w > 7$ earthquakes. These earthquakes involve coseismic slip on shallowly
78 dipping segments, despite the abundance of velocity-strengthening gouges in the youngest and
79 shallowest portions of exhumed LANF cores (Numelin et al., 2007b; Smith & Faulkner, 2010;
80 Niemeijer & Collettini, 2014; Mizera et al., 2020; Biemiller et al., 2020b).

81 Regardless of their tectonic and mechanical origins, active LANFs may pose significant
82 seismic hazards to nearby communities due to the possibility of strong ground motion,
83 landslides, and/or tsunamis associated with large LANF earthquakes (e.g., Cummins et al.,
84 2020). Further constraints on the physics of LANF earthquakes and the mechanical conditions
85 promoting shallow coseismic slip are needed to improve estimates of the seismic hazard
86 potential of these faults. Here, we develop data-constrained 3D numerical dynamic rupture
87 models of a well-documented active LANF, the Mai'iu normal fault in Papua New Guinea
88 (Figure 1). We characterize the dynamics and kinematics of LANF earthquake scenarios and
89 investigate stress and strength conditions that promote or inhibit seismic slip on these faults. In
90 particular, we examine rupture scenarios arising from geologically and geophysically inferred

91 loading and fault strength conditions. We find that such constrained 3D simulations generate
92 surface displacements similar to those recorded paleoseismically. We specifically analyze the
93 factors controlling whether coseismic slip penetrates the shallow velocity-strengthening region
94 during large LANF earthquakes.

95

96 1.2 Static and dynamic strength and loading of seismogenic LANFs

97 The 3D states of stress and effective fault strengths allowing seismic or aseismic LANF
98 activity are difficult to quantify and heavily debated (e.g., Yin, 1989; Spencer & Chase, 1989;
99 Yin et al, 1992; Axen, 1992, 2004, 2020; Buck, 1993; Wernicke, 1995; Abers et al., 1997;
100 Collettini & Sibson, 2001; Westaway, 2005; Collettini, 2011). Major outstanding questions
101 include; Are LANFs actually misoriented for slip, or does fault weakness explain the apparent
102 mechanical paradox? Can LANFs remain active under Andersonian conditions, or do they
103 require rotated principal stresses? Do shallow normal fault dips reflect low static frictional
104 strength, or can LANFs form in strong crust and retain their strength? Are seismogenic LANFs
105 critically stressed, or can sub-critically stressed segments rupture coseismically?

106 Dynamic rupture models provide self-consistent earthquake descriptions by
107 simultaneously simulating the physical processes that govern fault yielding, coseismic slip, and
108 seismic wave propagation. Data-integrated dynamic earthquake analysis can complement data-
109 driven approaches including complex and/or poorly instrumented events in various tectonic
110 contexts (e.g., Olsen et al., 1997; Douilly et al., 2015; Kyriakopoulos et al., 2017; Wollherr et al.,
111 2019) to explore the physical conditions and processes behind enigmatic slip behaviors observed
112 in recent earthquakes (e.g., Ulrich et al., 2019b, 2021, Palgunadi, 2020), as well as to develop
113 and test realistic rupture scenarios for active faults that lack a modern record of large earthquakes
114 (e.g., Aochi & Ulrich, 2015; Ramos et al., 2021), which can inform seismic hazard assessment.

115 In this framework, faults can be stressed well below failure (with a ratio of shear to
116 normal stress, τ/σ_n , lower than static friction μ_s) almost everywhere along the fault, yet break
117 spontaneously. Only a small portion of the fault needs to reach failure to nucleate a rupture, and
118 slip can propagate into regions of velocity- or slip-strengthening frictional behavior (e.g.,
119 Kaneko et al., 2010; van Zelst et al., 2019; Ramos et al., 2021). However, few dynamic rupture
120 models exist for normal fault earthquakes and these are restricted to planar faults (Oglesby et al.,
121 1998, 2000, 2008; Aochi, 2018; Gallovic et al., 2019; Aochi & Twardzik, 2020; Tinti et al.,
122 2021); to the best of our knowledge dynamic rupture models have not been used to explore
123 conditions allowing LANF rupture.

124 Various mechanisms have been proposed to explain how LANFs remain
125 mechanically viable (e.g., Axen, 1992, 2004; Collettini, 2011) including elevated pore fluid

126 pressures, fault weakness controlled by clay-rich gouge materials with low static friction, and
127 rotated (non-Andersonian) principal stress orientations conducive to slip at shallower dips. On
128 the coseismic timescale, dynamically weak fault rocks may govern coseismic fault strength,
129 regardless of their static frictional strength. Laboratory friction experiments on exhumed low-
130 angle normal fault rocks from the Zuccale fault in Italy (Smith & Faulkner, 2010; Niemeijer &
131 Collettini, 2014), the Panamint Valley fault in California (Numelin et al., 2007b) and the Mai'iu
132 fault in Papua New Guinea (Biemiller et al., 2020) confirm that well-developed gouges in mature
133 LANFs are commonly weak ($\mu_s \leq 0.4$) and velocity-strengthening at shallow subsurface
134 conditions due to the abundance of compliant clay minerals like saponite. Such weak LANFs
135 may not be misoriented for reactivation and slip under Andersonian extensional stresses (e.g.,
136 Collettini, 2011; Abers, 2009), whereas stronger faults with Byerlee frictional strength may
137 require favorably rotated principal stresses to slip.

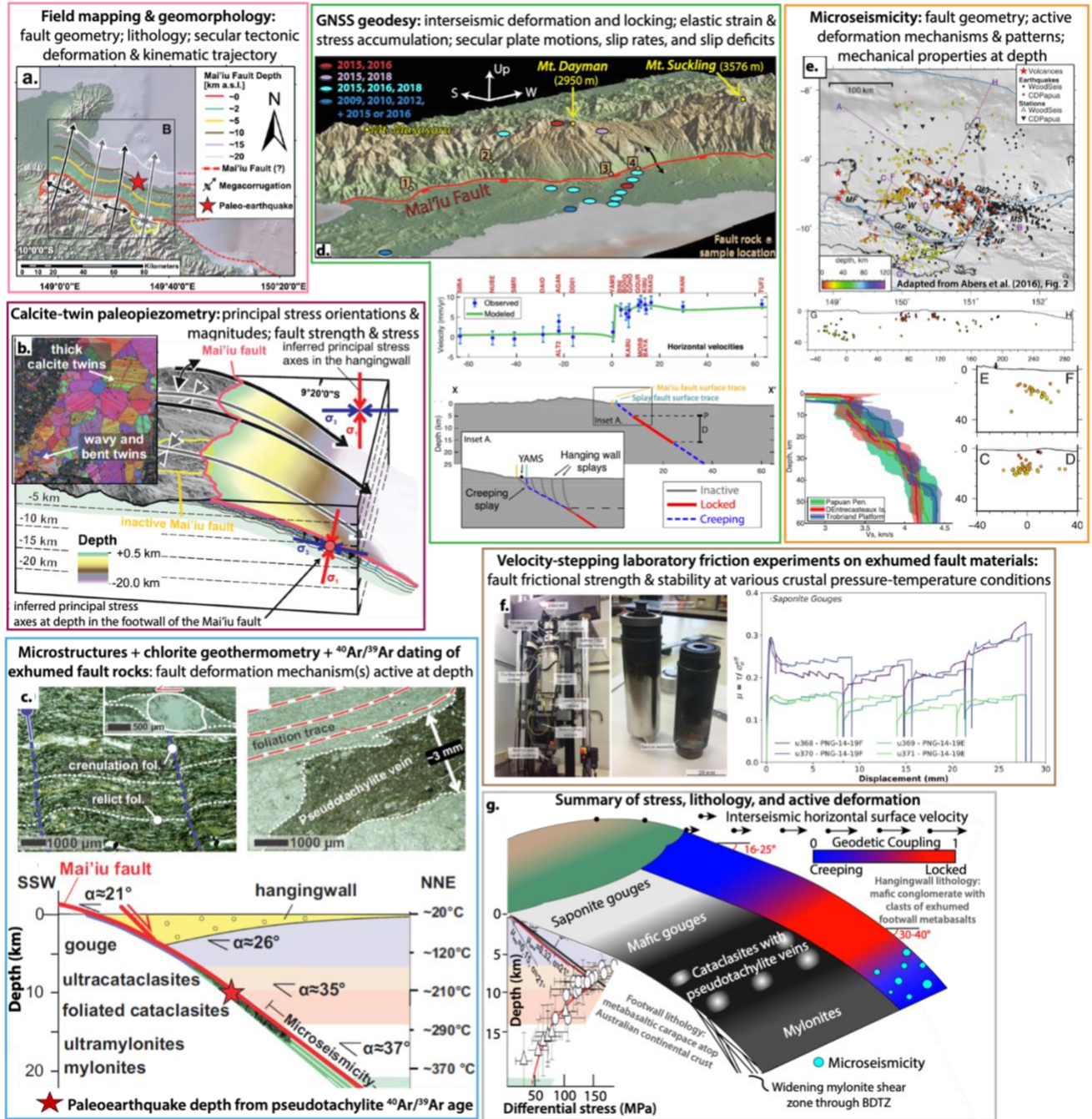
138 Principal stress orientations near LANFs remain disputed. Early models of LANF
139 formation invoked rotated principal stresses better oriented for shallow slip, with these
140 conditions either persisting throughout the crust or localized near the fault or the brittle-ductile
141 transition (e.g., Spencer & Chase, 1989; Yin, 1989, 1991; Melosh, 1990; Axen, 1992; Wernicke,
142 1995). Subsequent geodynamic models showed that long-term strain-dependent fault weakening
143 could facilitate flexural rotation of the footwall via a rolling-hinge, a long-term geodynamic
144 mechanism invoked to explain the formation and exhumation of metamorphic core complexes in
145 the back-rotated footwalls of detachment faults. This may explain the protracted mechanical
146 viability of normal faults dipping shallowly in the upper few km of the crust subject to
147 Andersonian extensional loading (Lavie et al., 1999, 2000). Two recent examples highlight the
148 ongoing discourse about different possible stress orientations around LANFs. Structural analysis
149 of the Whipple detachment in the southwest United States (Axen, 2020) suggests that it initiated
150 and slipped as a statically strong ($0.6 \leq \mu_s \leq 0.85$) fault under the influence of local non-
151 Andersonian stresses with a favorably rotated maximum principal stress, σ_1 , that plunges $\sim 45^\circ$ in
152 the dip-direction. In contrast, Mizera et al. (2021) jointly inverted paleostress orientations
153 recorded by calcite twins in the exhumed footwall of the Mai'iu fault along with the orientations
154 of smaller faults in its footwall and hanging wall to infer principal stress orientations in both
155 sections. Their analysis (Figure 1b) found that the hanging wall is characterized by extensional
156 Andersonian stresses with a vertical maximum principal stress and a horizontal minimum
157 principal stress aligned parallel to extension. In the footwall, σ_1 instead appears to be rotated
158 $\sim 15\text{-}20^\circ$ back towards the fault surface, implying that this LANF is even more misoriented for
159 slip in the footwall stress field than it is under standard Andersonian stress conditions.

160 Mechanical feedback between fault strength and the orientations and amplitudes of
161 tectonic stresses influences not only the long-term structural evolution of fault zones, but also the
162 interseismic, coseismic, and postseismic slip behaviors of active faults. In this study, we develop

163 data-constrained dynamic rupture scenarios to examine how these different tectonic stress
164 conditions affect coseismic rupture characteristics of an active LANF. Recent 3D dynamic
165 rupture models incorporating realistic tectonic stress conditions and complex fault geometries
166 confirm that regional stress orientations are a key factor controlling the dynamic viability of
167 coseismic slip (Palgunadi et al., 2020; Ulrich et al., 2021).

168 The inherent kinematic asymmetry of normal and reverse dipping faults has been shown
169 to lead to distinct dynamic rupture behaviors, such as reduced or enhanced shallow coseismic
170 slip. Aochi (2018) simulated ruptures under extensional and compressional loading conditions
171 constrained by Mohr-Coulomb failure criteria and linear slip-weakening friction. They observed
172 first-order differences in near-surface rupture characteristics between normal and reverse faults.
173 Reduced shallow normal fault slip was attributed to limited shallow shear stress accumulation in
174 these models, resulting from the inherently lower static (Mohr-Coulomb) strength of crustal
175 materials under extension relative to compression. Additionally, dip-angle-dependent shallow
176 clamping or unclamping can occur during normal fault earthquakes due to dynamic stress
177 interactions with the free surface above the shallowest portions of a rupturing normal fault
178 (Oglesby et al., 1998, 2000).

179



180

181

182

183

184

185

186

187

188

Figure 1. Summary of observations of Mai'iu fault structure and deformation that can constrain dynamic rupture modeling parameters, initial conditions, or model validation. See references and sections 2.3, 2.4, and 4.1 for more details. Modified from the following references: a.) Mapping confirms shallow dips of 16-24° and geomorphic analysis of fault remnants exhumed atop the corrugated footwall reveals rolling-hinge-style exhumation and ongoing along-strike contraction (Little et al., 2019; Mizera et al., 2019; Webber et al., 2020). b.) Inversion of paleostress orientations recorded by syntectonic calcite veins and minor faults indicate Andersonian stresses in the hanging wall and back-rotated principal stresses in the footwall (Mizera et al., 2021);

189 paleostresses indicate depth-dependent fault strength including a differential stress peak from ~6-
190 12 km depth (see panel g). c.) Exhumed fault rock microstructures preserve progressive sequence
191 of mixed frictional-viscous deformation including dislocation creep and seismic slip; chlorite
192 geothermometry provides temperature and depth constraints for this deformation sequence (Little
193 et al., 2019; Mizera et al., 2020). d.) Campaign GNSS measurements across the fault record
194 horizontal extension rates >8 mm/yr and suggest interseismic creep updip and downdip of a
195 strongly locked zone from ~5-13 km depth (Biemiller et al., 2020). e.) Planar-aligned
196 microseismicity offshore shows that from ~15-25 km depth the Mai'iu fault dips ~30-40° and
197 deforms by viscous creep accompanied by microseismic brittle failure; seismic velocity
198 modeling constrains depth-dependent temperature, density, and rigidity (Abers et al., 2016; Eilon
199 et al., 2015). f.) Velocity-stepping laboratory friction experiments on exhumed fault materials
200 reveal weak, velocity-strengthening saponitic gouges in the shallow fault zone ($<\sim 6$ km depth)
201 above stronger, velocity-weakening cataclastic rocks formed and deformed deeper (Biemiller et
202 al., 2020). g.) Summary figure showing inferred present-day deformation patterns and
203 mechanisms relative to lithological configuration and paleostress profile (Biemiller et al., 2020;
204 Mizera et al., 2021).

205

206 **2 Methods**

207 2.1 3D dynamic rupture modeling with SeisSol

208 Computational scenarios investigating LANF rupture dynamics must account for the
209 curved, shallowly dipping fault geometry and capture free-surface effects. We use SeisSol
210 (www.seissol.org) to solve the nonlinear coupled problem of spontaneous frictional failure and
211 seismic wave propagation. SeisSol uses fully non-uniform, statically adaptive, unstructured
212 tetrahedral meshes enabling geometrically complex models such as curved faults that intersect
213 the Earth's surface. Mesh resolution is adapted to ensure fine sampling of the faults while
214 satisfying the requirements regarding numerical dispersion of pure wave propagation away from
215 the fault (Figures 2a,b). End-to-end computational optimization (Heinecke et al., 2014;
216 Rettenberger et al., 2016; Uphoff et al., 2017), including an efficient local time-stepping
217 algorithm, allows for high efficiency on high-performance computing infrastructure. SeisSol is
218 verified in a wide range of community benchmarks (Pelties et al., 2014). SeisSol is freely
219 available (<https://github.com/SeisSol/SeisSol>).

220

221 2.2 Rate-and-state friction with enhanced velocity-weakening

222 Rate-and-state-dependent friction laws with enhanced velocity weakening allow faults to
223 operate at low average shear stress (Noda et al., 2009; Ulrich et al., 2019b). We use a regularized
224 formulation following Dunham et al. (2011) and Harris et al. (2018) as detailed in Supporting

225 Text S1. This formulation accounts for the rapid frictional weakening at coseismic slip rates
226 observed in high-velocity laboratory friction experiments (e.g., DiToro et al., 2011). Note that at
227 slip rates below the weakening velocity V_w , the frictional response to slip-rate variations is
228 governed by the rate-and-state friction parameters a and b . Materials with $a-b>0$ are velocity-
229 strengthening, with frictional strength increasing in response to increased slip rate, promoting
230 stable aseismic slip; those with $a-b<0$ are velocity-weakening and conditionally unstable, with
231 frictional strength decreasing in response to increased slip rate, potentially enabling unstable
232 seismic slip.

233

234 2.3 Data-constrained LANF reference model setup

235 We develop a LANF reference dynamic rupture model setup, in which we implement
236 physical conditions and mechanical properties inferred from recent observations of southeastern
237 Papua New Guinea and the Mai'iu fault system (Figure 2). These include Andersonian stresses
238 consistent with observationally constrained strike-perpendicular extension and strike-parallel
239 constriction. In subsequent models, we vary parameters such as prestress and fault friction to
240 assess how these conditions affect key dynamic rupture characteristics like the spatial extent and
241 rake of slip, surface uplift, seismic moment, total slip, peak slip rate, rupture speed and stress
242 drop. In this section we describe the reference model parameter choices (Figures 2, 3a; Table 1)
243 along with the field and laboratory evidence on which they are based.

244

245 2.3.1 Complex fault geometry

246 Our non-planar fault geometry (Figure 2a,b) is based on that of Webber et al. (2020), who
247 combined surface dip measurements with the microseismic data of Abers et al. (2016) to
248 constrain an interpolated subsurface model of the distinctively corrugated Mai'iu fault. Near the
249 base of the rapidly exhuming Mt. Dayman, the active fault geometry mirrors the concave-down
250 morphology of the domal footwall and exhumed fault surface of Mizera et al. (2019). Along-
251 strike to the southeast, the fault shallows and becomes concave-up beneath the Gwoira rider
252 block, a slice of the original hanging wall captured within the footwall of the active Gwoira splay
253 fault dipping $37-44^\circ$. Further southeast, the Mai'iu fault steps offshore where seismic reflection
254 data indicate pervasive normal faulting of its hanging wall basin (Fitz, 2011; Fitz & Mann,
255 2013a, 2013b), although the lack of surface exposure reduces the accuracy of the fault model
256 here.

257 Mesh resolution (Figure 2b) is statically adapted to ensure high enough fault resolution
258 (Text S2) and ranges from ~ 90 m to ~ 150 m. The full model domain is $1,000 \times 1,000 \times 500$ km³,
259 much larger than the $\sim 80 \times 70 \times 40$ km³ region of interest (Figures 2, 4b) to avoid any spurious
260 reflected waves from non-perfect absorbing boundaries. The top boundary is a flat free surface.
261 Automated unstructured tetrahedral mesh generation is performed with the software PUMGen

262 (<https://github.com/SeisSol/PUMGen/>), which also exports the mesh into the efficient PUMML
263 format used by SeisSol. PUMGen embeds MeshSim from SimMetrix, the underlying mesh
264 generator of SimModeler (www.simmatrix.com), such that the mesh generation may be run in
265 parallel on a compute cluster.

266

267 2.3.2 Fault frictional constitutive behaviour

268 Dramatic frictional weakening (Section 2.2) is the key mechanism governing dynamic
269 (co-seismic) fault weakness in our models. Rate-and-state friction parameters are based on those
270 measured by velocity-stepping laboratory friction experiments performed on various units of the
271 exhumed Mai'iu fault rock sequence under hydrothermal conditions analogous to a range of
272 crustal depths (Biemiller et al., 2020). Microstructural studies of these fault rocks revealed a
273 sequence of syn-extensionally deformed units progressing from the undeformed metabasaltic
274 protolith to ductilely sheared mylonites to frictional-viscously deformed cataclasites and
275 ultracataclasites to phyllosilicate-rich mafic and saponitic gouges (Little et al., 2019; Mizera et
276 al., 2020). Chlorite geothermometry provides constraints on the temperature and depth ranges
277 over which each fault rock unit deformed and accommodated a major component of fault slip
278 (Mizera et al., 2020). In our models, we map the measured a-b values of each unit to the
279 temperature-depth range over which it is inferred to have deformed (Figure 2c), following the
280 approach of slow slip cycle continuum models (e.g., Liu & Rice, 2007; Perez-Silva et al., 2021).
281 Above $\sim 300^{\circ}\text{C}$, the exhumed foliated cataclasites and mylonites are primarily velocity-
282 strengthening, and synextensionally formed microstructures indicate that viscous creep
283 mechanisms across a wider and less localized mylonitic shear zone accommodate most offset in
284 this regime. As such, from 15-17.5 km depth the weakening velocity V_w increases from the
285 standard value of 0.1 up to 1.0 (Figure 2d) to enhance the inferred velocity-strengthening
286 behavior at these depths. Additionally, we minimize any dynamic effects of the sharp corners of
287 the fault model geometry from Webber et al. (2020) by applying a 6-km-wide border of velocity-
288 strengthening material ($a-b = 0.006$; $V_w = 1.0$) at the along-strike terminations of the modeled
289 fault (Figure 2a).

290 Other friction parameters are constant as shown in Figure 2d. The maximum friction
291 coefficient reached during rupture is not a prescribed model parameter. Its value varies along the
292 fault and often exceeds our constant steady-state low-velocity friction coefficient $f_0=0.6$, but
293 rarely falls below this value. For simplicity, we use an estimated equivalent static friction
294 coefficient $\mu_s \approx f_0 = 0.6$ as a conservative value in the analysis of our simulation results and for
295 constraining prestress magnitudes (see Section 2.4).

296 Our assumed fully weakened friction coefficient, $f_w = 0.2$, is based on the minimum
297 experimentally measured effective friction in the velocity-weakening units of the exhumed
298 Mai'iu fault rock sequence (Biemiller et al., 2020a) and falls within the range of values typically

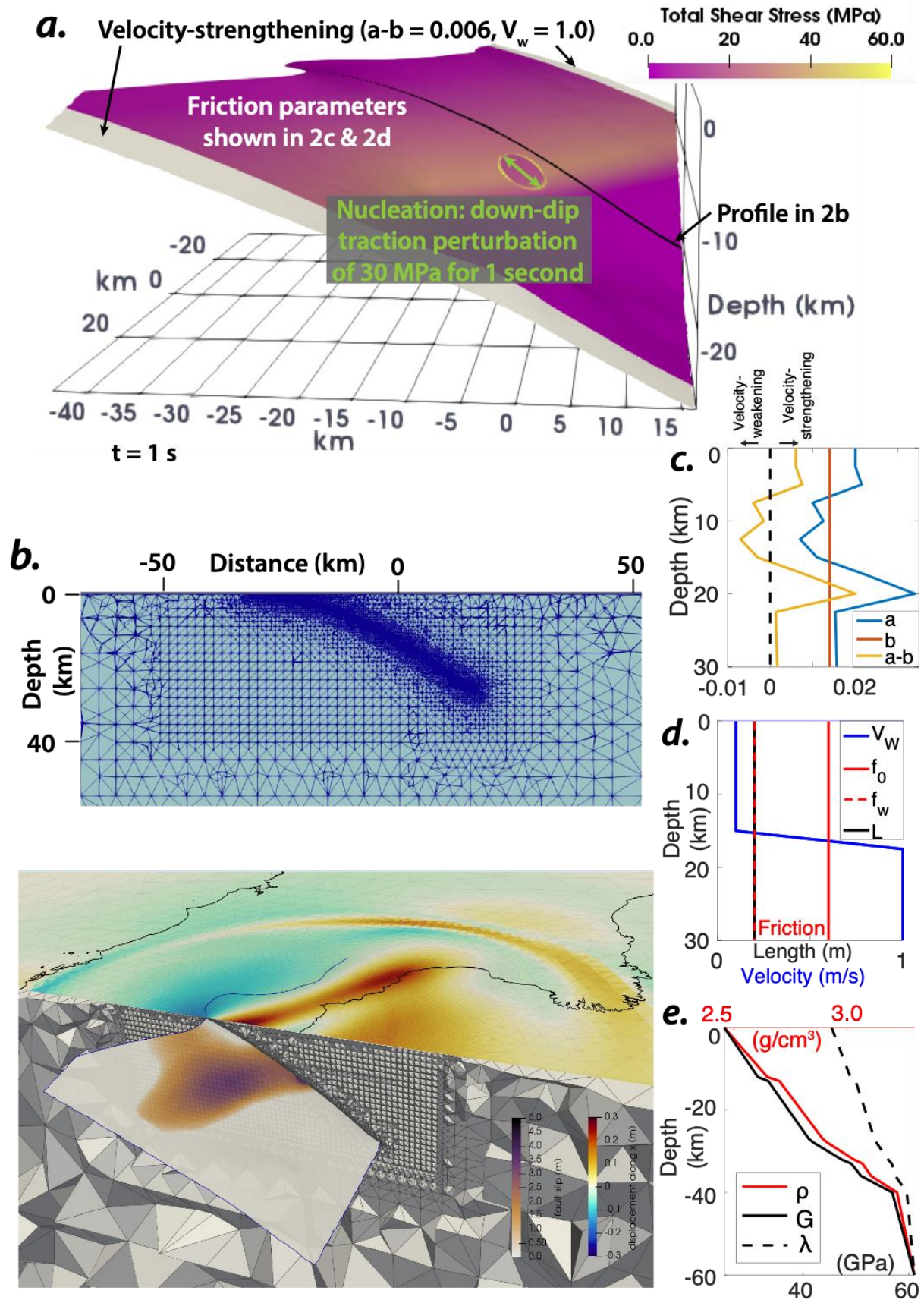
299 used in dynamic rupture earthquake models that reproduce rupture complexities, such as rupture
300 reactivation and pulse-like ruptures, without assuming small-scale heterogeneities (Noda et al.,
301 2009; Gabriel et al., 2012; Shi & Day, 2013; Palgunadi et al., 2020).

302

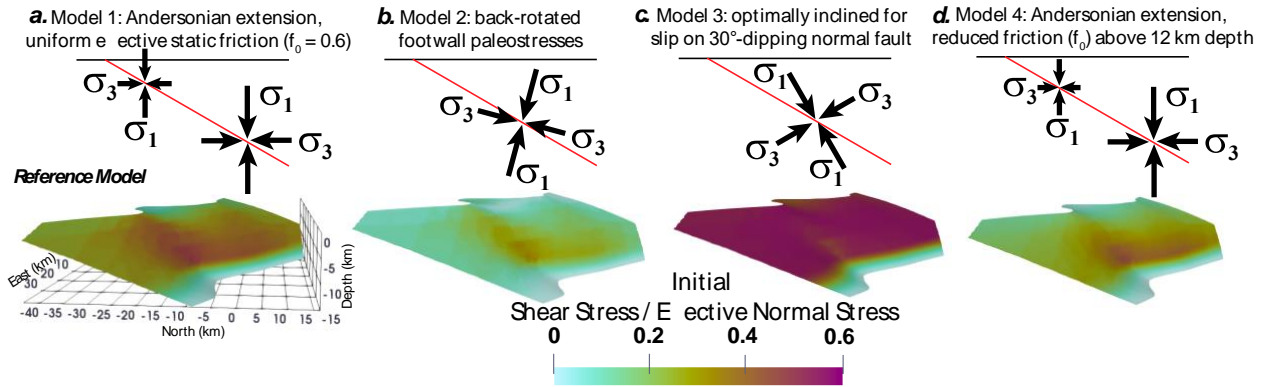
303 2.3.3. Regional lithological structure

304 Depth-dependent density (ρ) and elastic moduli (shear modulus G , Lamé parameter λ)
305 (Figure 2e) are derived from the Papuan Peninsula seismic velocity models of Abers et al. (2016)
306 and Eilon et al. (2015) in which V_s ranges from 3.2 km/s at 3 km depth to 4.3 km/s at 60 km
307 depth with associated V_p ranging from 5.8 km/s to 7.7 km/s. Following microstructural analyses
308 that show little evidence of sustained overpressures in the fault core (Little et al., 2019; Mizera et
309 al., 2020), our models use a modest pore fluid pressure ratio, $\lambda_f = P_f/\rho g z$, of 0.66 unless
310 otherwise noted.

311



313 **Figure 2.** LANF reference dynamic rupture model setup. See sections 2.3-2.5 of the text for
 314 details. a.) Shear stress after 1 s in model 1, highlighting the overstressed nucleation zone (green
 315 arrows, Section 2.5) and along-strike velocity-strengthening borders (gray). b.) Cross-sections of
 316 SeisSol’s unstructured tetrahedral computational mesh showing representative near-fault
 317 refinement. c-d.) Depth-dependence of fast-velocity weakening rate-and-state friction
 318 parameters. e.) Depth-dependence of density and elastic moduli.



321 **Figure 3.** a-d.) Schematic of principal stress orientations (above) and ratios of initial shear to
 322 effective normal stress, reflecting slip tendency (below) in models 1-4, respectively. We can
 323 consider f_0 as an estimate of the static friction coefficient (see Sections 2.3.2 and 2.4). Thus, the
 324 fault is initially close to failure when its apparent strength (initial shear over effective normal
 325 stress) is close to ~ 0.6 (except in model 4 at shallow depth, where a reduced f_0 is assumed in the
 326 computation of initial fault stress).

328

Model #	Figure #	T_{nuc} (MPa)	r_{nuc} (km)	R_0	λ_f	f_0	Stress	Plunge of σ_1 ($^\circ$)	Plunge direction of σ_1	M_w	Fault geometry
							Andersonian extension with constant μ_s^* , unless noted				Webber et al. (2020) unless noted
1	3, 4	30	2	0.95	0.66	0.6		90		7.14	
2	4	45	3	0.95	0.66	0.6	Footwall paleostresses: backwards-inclined σ_1	15	S30°W	6.42	
3	4	30	2	0.95	0.66	0.6	Inclined σ_1 well-oriented for LANF slip	30	N30°E	7.79	
4	4	30	2	0.95	0.66	0.2-0.6	Andersonian extension with depth-varying μ_s^*	90		6.88	

329

330 **Table 1.** Parameters varied in dynamic rupture simulation scenarios: maximum magnitude of
 331 nucleation overstress T_{nuc} , nucleation radius r_{nuc} , initial prestress ratio R_0 (equation 1), pore fluid
 332 pressure ratio λ_f (section 2.3.3), effective static friction f_0 , and resulting earthquake magnitude
 333 M_w .

334

335 **2.4 Regional stress constraints and LANF loading**

336 We simulate ruptures under different prestress conditions (Table 1) including
 337 Andersonian extension (Figure 3a,d) and stress fields where the maximum principal stress is
 338 non-vertical and plunges towards or away from the dip-slip direction (Figure 3b,c). Paleostress
 339 inversions (Mizera et al., 2021) and ongoing folding of the megacorrugated footwall (Little et al.,
 340 2019; Webber et al., 2020) indicate that strike-perpendicular extension is accompanied by strike-
 341 parallel constriction. The reference model, model 1 (Figure 3a, Table 1), employs an
 342 Andersonian stress field with the intermediate principal stress σ_2 oriented along-strike (N60W)
 343 resulting in the minimum principal stress σ_3 aligned parallel to the extension direction (N30E).
 344 The relative magnitudes of the principal stresses can be quantified by the stress-shape ratio, $\Phi =$
 345 $\frac{\sigma_2 - \sigma_3}{\sigma_1 - \sigma_3}$, where Φ ranges from 0 (axial compression) to 1 (axial constriction). Following Mizera et
 346 al. (2021) who report strongly constrictional stresses, we assume $\Phi = 0.8$ in all models.

347 How close any patch on the fault is to failure can be expressed by its apparent strength,
 348 the closeness of the ratio of initial shear stress over effective normal stress to an estimated
 349 equivalent static friction coefficient $\mu_s \approx f_0 = 0.6$ (Fig. 3) following Mohr-Coulomb theory. This
 350 apparent strength of the fault can be related to dynamic parameters which constrain the
 351 magnitude of deviatoric stresses (Ulrich et al., 2019b). We define the relative prestress ratio, R
 352 (Aochi & Madariaga, 2003), which is the ratio of the potential stress drop, $\Delta\tau$, to the full
 353 breakdown strength drop, $\Delta\tau_b$:

$$354 \quad R = \frac{\Delta\tau}{\Delta\tau_b} = \frac{\tau_0 - \mu_d \sigma_n'}{(\mu_s - \mu_d) \sigma_n'} \approx \frac{\tau_0 - f_w \sigma_n'}{(f_0 - f_w) \sigma_n'} \quad (1)$$

355 where τ_0 is the initial shear stress, σ_n' is the initial effective normal stress, $\mu_s \approx f_0$ is the
 356 estimated equivalent static friction coefficient and $\mu_d \approx f_w$ is the estimated equivalent dynamic
 357 friction coefficient. To compute R we assume $\mu_d = f_w = 0.2$, as we observe that fully weakened
 358 friction is typically reached. R is a relative fault strength defined with respect to the frictional
 359 strength drop. We prescribe only the maximum prestress ratio, R_0 , which is the prestress ratio of
 360 an optimally oriented fault in the stress field. Local fault orientation controls the initial prestress
 361 at any point on the fault, with $R \leq R_0$. For $R = R_0$, the fault segment is optimally oriented with
 362 respect to the local stress conditions. For $R_0 = 1$ an optimally oriented fault segment is also
 363 critically stressed.

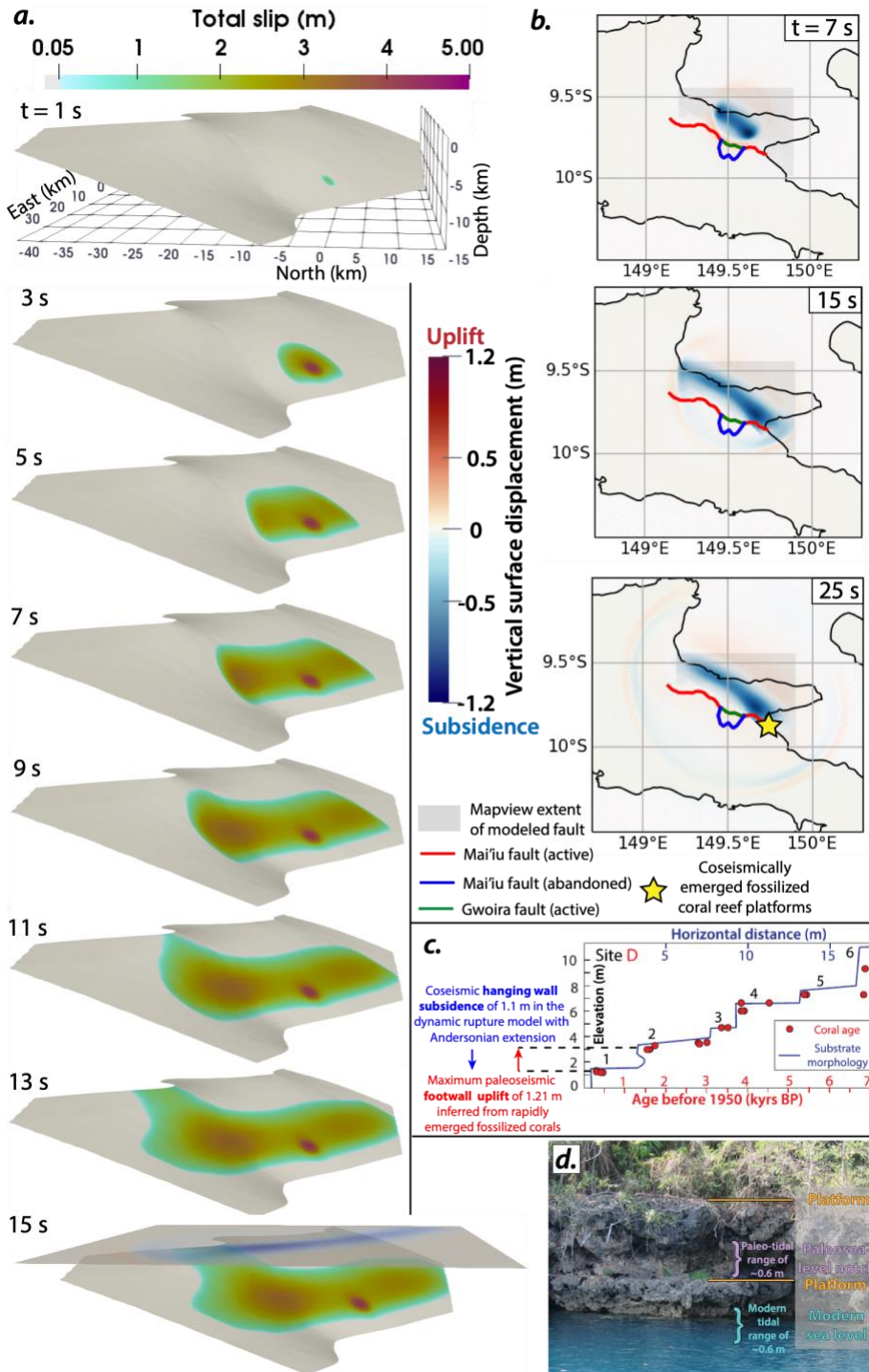
364 Stress magnitudes for each simulation are computed using observations following the
 365 approach of Ulrich et al. (2019b) assuming normal-sense dip-slip based on Φ , λ_f , R_0 , the azimuth
 366 of σ_2 , and the frictional strength of the fault given by f_0 . In Models 1-4, $R_0 = 0.95$, $\lambda_f = 0.66$, $\Phi =$
 367 0.8 , and σ_2 strikes N60W. Model variants with lower R_0 and λ_f (Figures S1, S2) require larger
 368 nucleation overstresses to rupture past the nucleation zone, but generally exhibit slip patterns
 369 similar to the reference model, highlighting the prevalence of these rupture characteristics over a
 370 wide range of initial conditions. We apply a smooth depth-dependent deviatoric stress taper to
 371 account for viscous creep below the brittle-ductile transition zone that limits the accumulation of

372 elastic strains and deviatoric stresses around deeper portions of the shear zone during the
373 interseismic period. We apply this taper from 11-15 km depth based on diffusion creep and
374 grain-boundary sliding recorded microstructurally in the fault rocks deformed below the
375 paleopiezometrically determined fault strength peak from 6-12 km depth (Mizera et al., 2020,
376 2021).

377

378 2.5 Earthquake nucleation

379 Earthquakes in dynamic rupture models can be nucleated in a variety of ways. We aim
380 for the nucleation procedure that requires the smallest perturbation in order to minimize artificial
381 effects of the nucleation conditions on rupture behavior (e.g., Galis et al., 2015). We nucleate
382 slip at a reasonable location on the fault based on available data. Nucleation is commonly
383 imposed through a temporary local reduction of fault frictional strength (e.g., Wollherr et al.,
384 2019; Harris et al., 2021; Tinti et al., 2021), or via temporary local increased stresses (e.g., Galis
385 et al., 2015; Ulrich et al., 2019b). Here, we impose a temporary increase in the down-dip shear
386 traction on the fault (T_{nuc}) that evolves smoothly in both space and time over a spherical region
387 of radius r_{nuc} and a nucleation duration t_{nuc} . We assume earthquakes on the Mai'iu fault are most
388 likely to nucleate in the strong velocity-weakening cataclastic fault rocks in the vicinity of the
389 paleopiezometric stress and strength peak and the geodetically locked zone, around 10-12 km
390 depth. Thus, we apply the nucleation conditions in a central location along-strike centered at a
391 depth of 11 km. Through trial-and-error, we derive the smallest possible shear traction
392 perturbation that leads to rupture propagation in most models, using T_{nuc} of 30 MPa, r_{nuc} of 2 km,
393 and t_{nuc} of 1 second.



394
 395 **Figure 4.** Temporal evolution of a.) fault slip and b.) vertical surface displacement in the
 396 reference model. The last snapshot at 15s simulation time in a) includes a perspective view of the
 397 accumulated vertical surface displacement. The gray shaded rectangular area in b) is the
 398 mapview area of our full modeled fault geometry (full fault model domain shown in Figure 2a).
 399 c.) Magnitudes of modeled coseismic hanging-wall subsidence of $\sim 1\text{ m}$ (blue arrow) beneath
 400 Goodenough Bay are similar to maximum paleoseismic displacements (red arrow) inferred from

401 episodically emerged fossilized coral platforms found there, as shown by the elevations and
402 U/Th ages of d.) sampled platforms from Western Goodenough Bay (from Biemiller et al.,
403 2020a).

404

405 **3. Results**

406 In the following sections we describe four key LANF dynamic rupture models including
407 one preferred reference model. In the Supporting Information we detail additional results from
408 dynamic rupture simulations probing model sensitivity, including models with alternate pre-
409 stresses that are initially farther from failure, models with alternate pore fluid pressures, variants
410 of model 3 with stronger imposed nucleation conditions, models with planar detachment fault
411 geometries, and models without velocity-strengthening materials in the shallow parts of the fault
412 (Table S1, Figures S1-S5).

413

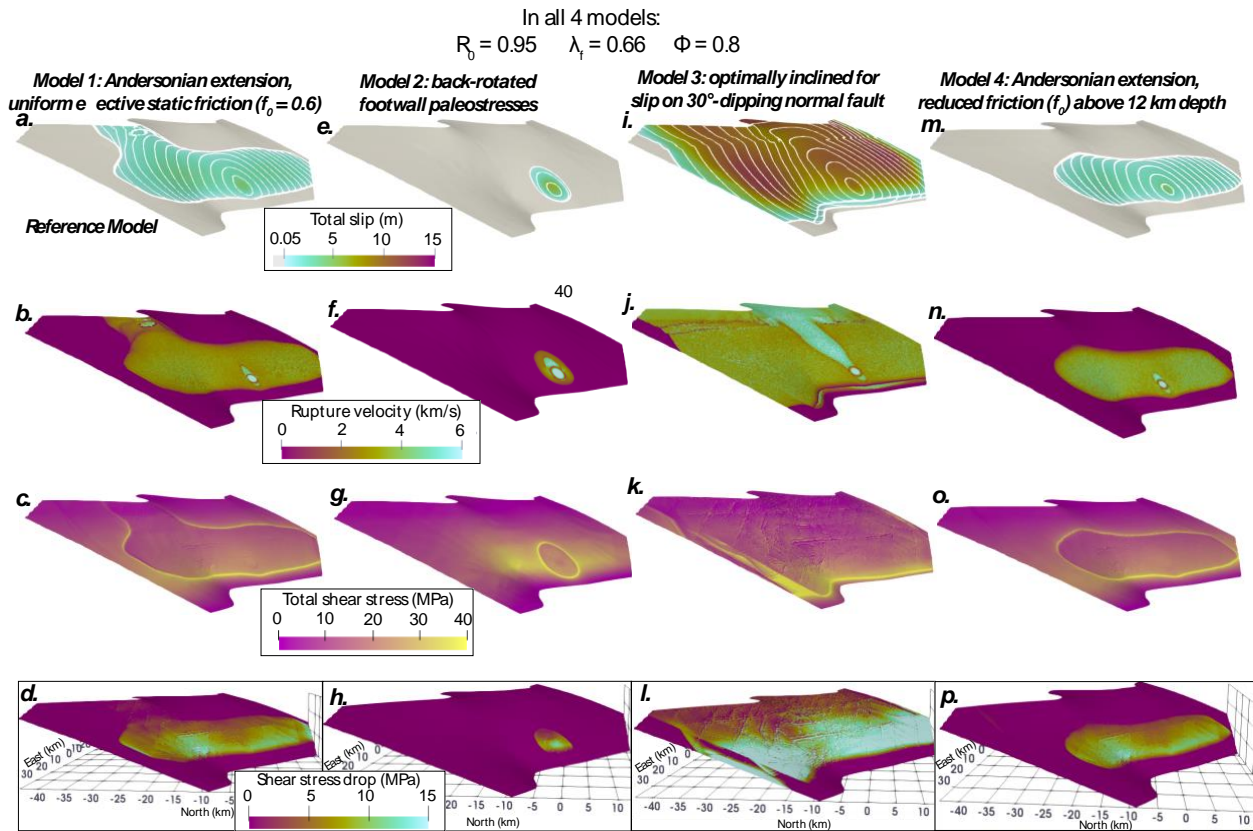
414 3.1 Reference model based on inferred hanging-wall stresses: Andersonian extension and
415 uniform fault static friction $f_0 = 0.6$

416 Figures 4a and 4b show the evolution of fault slip and vertical surface displacement over
417 15 s of the simulated M_w 7.1 earthquake in the reference model. Figures 5a-d summarize
418 accumulated fault slip, rupture velocity, total shear stress and stress drop which we estimate as
419 the difference between the initial (at $t=0$ s) and final total shear stress after 15 seconds simulation
420 time. Model 1 is loaded with Andersonian extensional stresses, as inferred from paleostress
421 analysis of hanging-wall faults (Mizera et al., 2021), computed for Byerlee frictional fault
422 strength assuming uniform $f_0 = 0.6$ (Figure 3a; Table 1). The imposed nucleation traction
423 perturbation lasts one second, and subsequent rupture is spontaneous and self-sustained. Rupture
424 initially propagates updip towards the surface and in both directions along-strike, but arrests
425 downdip near the deviatoric stress taper and the transition to velocity-strengthening fault
426 materials. In the western portion of the fault downdip of Mt. Dayman, updip rupture propagation
427 is arrested at around 5 km depth, near the transition to shallow velocity-strengthening gouges. In
428 contrast, rupture penetrates the shallow velocity-strengthening portion of the eastern segment
429 along Goodenough Bay resulting in 1-2 m of slip at the surface. Lateral rupture propagation
430 proceeds along-strike in both directions within the velocity-weakening units between 5-13 km
431 depth until reaching the edges of the modeled fault, where imposed velocity-strengthening
432 borders arrest rupture. Rupture propagates at 3-4 km/s rupture velocity on most of the slipped
433 fault (Figure 5b), but briefly reaches supershear speeds approaching the assumed respective local
434 P-wave velocities ranging from 6.3 km/s close to the hypocentre to 5.8 km/s near the free
435 surface. Supershear rupture remains localized within ~ 1 km of the nucleation zone and in a small
436 patch of the shallow Goodenough segment, where unsustained supershear slip initiates slightly
437 ahead of the main rupture front (Kaneko & Lapusta, 2010). Between 6-13 km depth, stress drops

438 range from 4-11 MPa (Figure 5d), while in the shallow slipped portion stress drops are limited to
 439 <3 MPa, which is a consequence of the linear depth-dependence of the initial loading.

440 Coseismic vertical surface displacements are punctuated by dynamic along-strike and
 441 counter-dip-direction propagation of a surface-wave-mediated uplift front, 30-40 cm high, that
 442 initiates atop the hanging wall, followed closely by along-strike propagation of a more
 443 pronounced pattern of subsidence in the hanging wall which outlines the final static displacement
 444 pattern of hanging wall subsidence of up to 1.1 m. Static footwall uplift occurs only at the trace
 445 of the Goodenough segment and is limited to < 3 cm. With observationally constrained
 446 mechanical properties and fault geometry subject to stresses consistent with structurally inferred
 447 hanging-wall stresses, this model generates coseismic vertical surface displacements in western
 448 Goodenough Bay similar to paleoseismic offsets inferred from rapidly emerged fossilized coral
 449 platforms there (Figure 4b-d; see section 4.1 for details). Thus, Model 1 is a compelling and
 450 appropriate reference model against which to compare results from other rupture scenarios.

451



452

453 **Figure 5.** Results after 15 seconds for models 1 (a-d), 2 (e-h), 3 (i-l) and 4 (m-p). Top row: Total
 454 slip (m) with white rupture contours plotted every 1 s. Second row: Rupture velocity (km/s).
 455 Localized supershear rupture episodes appear as light blue, e.g. updip of the nucleation zone in
 456 model 3. Third row: Postseismic shear stress. Shallow stress concentrations updip of a buried

457 rupture patch (c,o) may promote shallow afterslip or interseismic creep (see Discussion). Bottom
458 row: modelled stress drop (MPa) estimated as the change in total shear stress from $t=0s$ to $t=15s$.
459

460 3.2 Model 2: inclined principal stress orientations inferred from syntectonic calcite veins 461 in the exhumed footwall

462 The setup of Model 2 is identical to the reference model except that initial stresses are
463 calculated based on a σ_1 orientation plunging 15° SSW, now consistent with the
464 paleopiezometrically inferred footwall stress orientations (Mizera et al., 2021) and optimally
465 oriented for dip-slip on a normal fault dipping 75° . With such backwards-inclined principal
466 stresses, LANFs should be even less well-aligned for slip than they are under Andersonian
467 conditions, as illustrated by the decreased ratio of initial shear stress over initial effective normal
468 stress (Figure 3b). With identical imposed nucleation tractions to those that generate a M_w 7.1
469 event in the reference model, rupture fails to nucleate under these rotated principal stress
470 conditions and slip remains limited to the predefined nucleation patch. Increasing the magnitude
471 and area of the imposed overstress results in more slip in and around the nucleation zone, but
472 does not lead to a dynamically viable model with rupture propagating onto other parts of the fault
473 (Figure S3). For example, the panels in Figure 5 associated with model 2 result from a model
474 with 50% increased nucleation conditions ($T_{nuc} = 45$ MPa, $r_{nuc} = 3$ km), yet slip remains limited
475 to within a few km of the nucleation zone. R_0 is already close to 1 in models 1-4 and cannot be
476 increased further to enhance slip tendency and promote unstable slip. Thus, these backwards-
477 inclined principal stress orientations appear to be incompatible with any dynamically viable
478 rupture scenarios.

479

480 3.3 Model 3: inclined principal stress orientations aligned optimally for dip-slip on a 481 normal fault dipping 30°

482 Many models for LANF formation propose that rotated principal stress orientations
483 through part or all of the crust establish a stress field conducive to normal-sense slip on
484 shallowly-dipping faults, with σ_1 plunging at a small angle to the detachment (e.g., Spencer &
485 Chase, 1989; Lister & Davis, 1989; Yin, 1989; Melosh, 1990). We test the dynamic effects of
486 such a stress field in model 3. Conditions in model 3 are identical to model 2 except that σ_1
487 plunges 30° in the opposite direction (NNE), such that it is more closely aligned with the dipping
488 fault. Such rotated stresses should be optimally aligned for normal-sense slip on a fault dipping
489 30° , as highlighted by the increased ratio of initial shear stress over initial effective normal stress
490 (Figure 3c). As in the reference model, rupture in model 3 initially propagates rapidly in all
491 directions except down-dip (Figure 5i); however, it subsequently accelerates updip rather than
492 arresting near the transition to velocity-strengthening material. After 7 s, slip penetrates to the
493 surface on the most shallowly-dipping segment beneath the Gwoira rider block. Subsequent

494 rupture propagates in both directions along-strike at all depths above ~14 km, saturating the
495 entire fault with slip and even rupturing into the strongly velocity-strengthening barriers at the
496 along-strike edges of the model. This M_w 7.8 earthquake results in maximum slip of more than
497 12 m, including up to 11 m of slip at the surface. Unlike the reference model, this event includes
498 localized but significant supershear rupture episodes directly updip of the nucleation zone
499 (Figure 5j). Modelled stress drops are larger than in Model 1, ranging from 15 MPa to more than
500 20 MPa between 6 and 13 km depth (Figure 5l).

501

502 3.4 Model 4: Andersonian extensional stresses adjusted for reduced near-surface static
503 effective friction ($0.25 \leq f_0 \leq 0.6$)

504 Finally, Model 4 considers decreased near-surface fault stress and strength conditions
505 implemented through reduced effective static friction f_0 above 12 km depth. Mechanical models
506 of LANF formation commonly invoke significant shallow fault weakening to explain how these
507 normal faults penetrate through the upper crust and remain active at such shallow dips (e.g.,
508 Axen, 1992; Collettini, 2011). In addition, geodynamic models that develop LANFs via footwall
509 rotation through a self-consistent rolling-hinge typically require finite strain-weakening
510 mechanisms. These reduce fault strength with continued slip and flexural rotation of the fault and
511 exhuming footwall, leading to very low effective fault strength near the surface (e.g., Buck,
512 1988; Lavier et al., 1999, 2000; Whitney et al., 2013). Possible brittle strain-weakening
513 mechanisms include loss of cohesion and precipitation of weak clay minerals during prolonged
514 slip, while viscous strain-weakening may occur via grain-size reduction and related strain
515 localization. Thus, it appears feasible that crustal stresses near such weak faults may be
516 modulated by local fault strength (Axen, 1992; Rice, 1992) and vary with depth based on fault
517 rock and gouge composition. In model 4, Andersonian extensional stresses are computed as in
518 the reference model, but assuming that the shallow equivalent static friction coefficient f_0
519 decreases linearly from 0.6 at 12 km depth to 0.25 at the surface following experimentally
520 measured friction coefficients of the exhumed Mai'iu fault rocks (Biemiller et al., 2020b). The
521 resulting earthquake mirrors most of the slip behavior of the reference model, but rupture notably
522 does not penetrate to the surface through the shallow velocity-strengthening region of any fault
523 segment. Instead, slip is limited to depths of ~6-13 km within a slightly narrower along-strike
524 region, resulting in less total slip everywhere during this smaller M_w 7.0 event.

525

526 4. Discussion

527

528 4.1 Integration of observations to constrain dynamic rupture modeling of LANF
529 earthquake scenarios

530 Initial conditions of dynamic rupture modeling include the preexisting state of stress and
531 the frictional properties governing fault strength and sliding, as well as the lithological structure
532 and fault geometries. We demonstrate how to integrate geophysical and geologic observations to
533 constrain all required initial conditions for realistic LANF earthquake scenarios. For example, we
534 impose a linearly decreasing deviatoric stress ramp from 11-15 km depth based on the
535 paleostress depth profile of Mizera et al. (2021), which successfully limits the downdip rupture
536 extent in all models to between 13-15 km depth, in line with both the geodetically inferred
537 downdip edge of interseismic locking and the updip extent of planar-aligned microseismicity
538 inferred to delineate the viscously creeping mylonitic shear zone. Our modelled earthquakes
539 agree with realistic levels of static and dynamic frictional resistance, slip, rupture speed and
540 stress drop and adopt a friction law with severe velocity weakening that enables complex rupture
541 and realistic amounts of slip, in contrast to simplified friction laws.

542

543 4.2 Implications of the reference model for the seismic cycle and hazard potential of the 544 Mai'iu fault

545 Geologic and geophysical evidence of past and ongoing Mai'iu fault deformation align
546 well with areas of the fault that dynamically slip in the reference model with strike-perpendicular
547 Andersonian extension in a constrictional stress field, modest pore fluid pressure, and high
548 closeness-to-failure for well-oriented fault segments. Although the same depth-dependent
549 frictional and mechanical properties are assumed uniformly along strike, rupture propagates to
550 the surface on the eastern Goodenough segment, but not on the central Gwoira segment, where
551 the capture and transport of the overlying Gwoira rider block indicates abandonment of the
552 shallowest portion of the Mai'iu fault (Little et al., 2019; Webber et al., 2020). We attribute these
553 preferential shallow rupture patterns to static and dynamic effects associated with the local fault
554 geometry: the Goodenough segment dips more steeply near the surface than the Gwoira or
555 Dayman segments. In terms of static fault mechanical viability, the more steeply-dipping
556 segments are better-oriented for normal slip. Co-seismically, rupture asymmetry and static and
557 dynamic stress interactions between a slipping normal fault and the free surface can either hinder
558 or promote near-surface rupture depending on the fault dip (Nielsen, 1998, Oglesby et al., 1998,
559 2000, 2008; Ma and Beroza, 2008).

560 Additional dynamic increase of shallow shear stresses close to the free-surface is caused
561 by trapped waves between the free-surface and the hanging-wall favoring shallow slip (e.g., van
562 Zelst et al., 2019). These combined static and dynamic effects promote shallow rupture by
563 dynamically weakening normal faults dipping 30° - 75° but impede shallow rupture on those
564 dipping less than 30° or more than 75° (Oglesby et al., 1998). This effect of fault dip on dynamic
565 rupture viability is highlighted and isolated in alternative models with planar detachments
566 dipping 25° and 35° (Figure S4): rupture fails to propagate more than a few km past the

567 nucleation zone on the 25°-dipping fault, whereas the entire 35°-dipping fault slips above ~12
568 km depth with rupture propagating to the surface everywhere.

569 Rupture on the Gwoira and Dayman segments notably arrests around 5 km depth, at the
570 updip edge of the geodetically inferred locked zone. This modeled rupture pattern raises the
571 interesting possibility that postseismic stress concentrations leftover from an earthquake may
572 drive shallow afterslip and/or interseismic creep updip of the area that slipped coseismically,
573 within the weak velocity-strengthening saponitic gouges found there. Figure 5 (third row)
574 illustrates modeled postseismic shear stress concentrations outlining the rupture areas, which in
575 Models 1 and 4 include large shear stress increases updip of the buried rupture patch that could
576 drive shallow afterslip or interseismic creep (Figure 5c,o). Additionally, shallower slip on all
577 segments in an alternate model with $a-b < 0$ above 15 km depth confirms the important stabilizing
578 role of the shallow velocity-strengthening gouges in limiting shallow coseismic slip (Figure S5).

579 Distinct platform-notch-platform sequences of fossilized coral reefs along the
580 southwestern Goodenough Bay shoreline indicate punctuated emergence events with average
581 maximum vertical displacements of 1.3 m (Figure 4c,d; Biemiller et al., 2020a). Rupture in the
582 reference model propagates to the surface on the segment directly below these emerged corals,
583 resulting in ~2 m of near-surface slip and static vertical coseismic offsets of up to 1.1 m (Figure
584 4). Interestingly, the modeled offsets consist almost entirely of hanging-wall subsidence with
585 only a few cm of footwall uplift. Based on the faceted coastal morphology and presence of older
586 fossilized corals at >300 m elevation (Mann & Taylor, 2002; Mann et al., 2004, 2009), these
587 younger emerged coral platforms were previously interpreted as products of coseismic footwall
588 uplift during normal fault earthquakes (Biemiller et al., 2020a); however, our dynamic rupture
589 models suggest that these platform-notch sequences may form due to abrupt coseismic hanging
590 wall subsidence but emerge during more gradual footwall uplift that persists through most or all
591 of the seismic cycle. This process is more consistent with geodetically observed coseismic
592 vertical displacements from continental normal fault earthquakes, which typically show
593 pronounced hanging wall subsidence and minor-to-moderate footwall uplift (e.g., Stein &
594 Barrientos, 1985; Cheloni et al., 2017). Additionally, gradual emergence may explain the poor
595 along-strike preservation of these pronounced platforms: only the largest platforms on the most
596 rapidly uplifting parts of the coastline can survive the intense erosion they experience during
597 gradual emergence through the intertidal zone.

598

599 4.3 Stress orientations near seismogenic detachment faults

600 Our results suggest that active detachment faults can host moderate ($M_w > 7$) earthquakes
601 within Andersonian stress fields and that these earthquakes may not necessarily rupture to the
602 surface. Near-surface rupture may be impeded by the geometric effect of gentler fault dips, the
603 stabilizing effect of clay-rich gouges, and/or the interaction of dynamic stress perturbations with

604 the free-surface above a rupturing normal fault (Nielsen, 1998; Oglesby et al., 1998, 2000;
605 Aochi, 2018). Additionally, model 4 considers the possibility of decreased near-surface fault
606 stress and strength conditions associated with a near-surface reduction of effective static friction
607 f_0 . Interseismic creep on the weak shallow portion of a mature detachment may reduce the
608 effective shear stress there, further limiting its propensity for shallow rupture. These results are
609 encouraging in terms of the hazard potential of detachments, as surface-rupturing earthquakes
610 are commonly the most damaging and tsunamigenic; however, we note that our models do not
611 include any steeply-dipping splay faults in the hanging wall, which may be better-aligned for
612 reactivation and generate more coseismic uplift and subsidence due to their steeper geometry.
613 Future modeling work could assess the hazard potential of complex detachment systems with
614 splay-faulted hanging walls. Additionally, continuous high-resolution postseismic geodetic
615 monitoring of near-fault displacements following buried rupture of a normal fault could test
616 whether postseismic stress concentrations drive shallow afterslip updip of the rupture patch.

617 Detachment faults commonly juxtapose strong metamorphic footwall rocks against
618 weaker sedimentary rocks in the hanging wall (e.g., Whitney et al., 2013), but the effect of such
619 strength contrasts on the interseismic loading of these faults remains unclear. Failed nucleation in
620 Model 2 implies that applied stresses on the Mai'iu fault are more similar to those in its hanging
621 wall than its footwall, suggesting that effective stress on the seismogenic portions of detachments
622 may be limited by the strength of the hanging wall, which is typically lower than that of the
623 metamorphic footwall due to the presence of weaker, less consolidated, unmetamorphosed
624 sedimentary rocks. Additionally, stresses in the footwall and hanging wall may be largely
625 decoupled if the detachment is weak, as suggested by paleopiezometry and geodynamic models
626 of the Mai'iu fault (Biemiller et al., 2019; Mizera et al., 2021), not unlike local stress orientation
627 heterogeneities observed in the shallow subduction margins of Nankai (Lin et al., 2016) and
628 Hikurangi (McNamara et al., 2021) which may be tied to effective stress and pore pressure
629 discontinuities across the weak, impermeable shallow subduction interface fault zones (e.g.,
630 Skarbek & Saffer, 2009).

631 Although rotated principal stresses better-aligned for low-angle normal-sense slip have
632 been proposed for some LANFs, we find that these conditions are not necessary to explain
633 continued slip on these faults, as highlighted by recent fault reactivation analyses (e.g., Abers,
634 2009; Collettini, 2011). If any detachment faults formed and remain active within optimally
635 inclined stress fields, these are certainly the most likely to host large ($M_w > 8$) damaging
636 earthquakes (Figure 5i); however, these stress conditions do not appear to be common or
637 representative of most extensional settings. Our dynamic rupture scenario with well-aligned
638 principal stresses features high stress drops (> 15 MPa; Figure 5l) and supershear rupture
639 velocities (larger than the seismic shear wave velocity; Figure 5j). Sustained supershear rupture
640 transition is associated with larger relative prestress ratio R_0 (e.g., Dunham et al., 2007; Gabriel

641 et al., 2012). The expected stress drop in our models can be estimated to first order as $(1 -$
642 $\lambda_f)\sigma_n'(\mu_s - \mu_d)R_0$ (Ulrich et al., 2019b) which in model 4, for example, increases from 0 MPa at the
643 surface to 24 MPa at 15 km depth. Thus, both the dynamically modeled stress drop and the
644 rupture velocity could be decreased in models with lower R_0 ; however, low R_0 would hinder
645 rupture nucleation on any segment and would imply that even well-oriented parts of the fault are
646 stressed far from criticality, which is at odds with observations from continental drilling (e.g.,
647 Townend & Zoback, 2000; Zoback & Townend, 2001) and post-glacial fault reactivation (e.g.,
648 Steffen & Steffen, 2021) that indicate the crust is critically stressed (e.g., Zoback & Zoback,
649 2007). Sibson (1990) distinguished two classes of misoriented faults: those that are *unfavorably*
650 *oriented* under Anderson-Byerlee conditions, and those that are *severely misoriented* and require
651 pore fluid pressures to exceed σ_3 for the fault to remain mechanically viable, breaching the so-
652 called ‘hydrofrac limit’ (e.g., Abers, 2009) at which deformation proceeds via the opening of
653 new hydrofractures rather than continued fault slip. Although the most shallowly dipping
654 portions of LANFs appear *unfavorably oriented* to Andersonian stresses, their local static
655 frictional weakness may keep them from being severely misoriented for long-term slip viability
656 by reducing the lock-up angle of their hydrofrac limit (e.g., Collettini, 2011), enabling dynamic
657 slip viability during ruptures nucleated on nearby segments that may be better-oriented. In the
658 case of the Mai’iu fault, steeper dips of 30-40° at seismogenic depths of 12-15 km indicate the
659 fault is better-oriented at depth and help explain the mechanical viability of rupture nucleation on
660 this fault.

661

662 4.4 LANF stress criticality and implications for ‘keystone’ faults and complex ruptures

663 Understanding whether LANFs must be critically stressed to slip coseismically could
664 help assess whether LANF segments control the interseismic strength and eventual seismic
665 failure of multi-fault detachment systems. Our dynamic rupture modeling explains how
666 coseismic slip can penetrate into unexpected parts of faults that do not appear well-primed for
667 seismic slip, like segments poorly-oriented relative to the regional stress field, areas with
668 velocity-strengthening behavior, and portions not initially stressed close to static frictional
669 failure. We note that Models 1-4 all include $R_0=0.95$, meaning that regardless of the given stress
670 orientation scenario, any fault segment well-oriented for slip in their respective stress field is
671 initially stressed close to failure. Under Andersonian extension, for example, more steeply-
672 dipping normal faults are expected to be stressed to failure and rupture coseismically before their
673 shallowly dipping counterparts. However, recent evidence from an active multi-fault detachment
674 system in Baja California suggests well-oriented faults near a low-angle detachment may be
675 stressed to failure without rupturing seismically until the underlying detachment is critically
676 stressed.

677 For the best-documented modern earthquake involving LANF slip, the 2010 M_w 7.2 El-
678 Mayor Cucapah event, Fletcher et al. (2016) proposed that the LANF segment acted
679 interseismically as the keystone fault, limiting seismic slip on an intersecting network of better-
680 oriented critically-stressed faults until eventually the poorly-oriented detachment was critically
681 stressed to failure. Model 3 with nearly critically-stressed conditions in the hypocentral region
682 generates our largest modeled earthquake and presents unusually large stress drops and
683 supershear rupture velocities, while our reference model is initially subcritically stressed at
684 hypocentral depths but generates coseismic surface displacements similar to those recorded
685 paleoseismically. Thus, our results suggest that LANFs can slip coseismically without being
686 interseismically critically stressed near their static frictional failure strength. Nonetheless, similar
687 to the keystone fault model, classically better-oriented detachment segments and neighboring
688 normal faults would be stressed closer to failure than the shallowly-dipping parts of the Mai'iu
689 fault in the Andersonian extensional stress field of the reference model.

690 Our models suggest that LANFs are dynamically viable under common crustal loading
691 conditions, yet they do not fully resolve the perplexing scarcity of large earthquakes with well-
692 resolved low-angle normal-sense focal mechanisms in the modern instrumental record (Jackson
693 & White, 1989; Collettini & Sibson, 2001), for which various mechanical explanations have
694 been proposed. Wernicke (1995) posited that LANF earthquakes are particularly rare because
695 these faults typically accommodate relatively slow extension rates (a few mm/yr) and thus host
696 only infrequent earthquakes; however, faster extension rates ≥ 1 cm/yr across the Mai'iu fault
697 (Wallace et al., 2014; Webber et al., 2018; Biemiller et al., 2020b) and the Banda detachment
698 (Cummins et al., 2020) suggest these LANFs should host more frequent earthquakes.
699 Nonetheless, paleoseismically recorded recurrence intervals from the Goodenough portion of the
700 Mai'iu fault range from 482 – 1590 years (Biemiller et al., 2020a). It is plausible that large
701 LANF earthquakes have not been recorded simply because their recurrence intervals are much
702 longer than the relatively short instrumental record. Building on the keystone fault model of
703 Fletcher et al. (2016), Karlsson (2021) proposed that if LANFs typically slip in complex multi-
704 fault ruptures that involve simultaneous slip on multiple steeply-dipping normal faults, then
705 seismic signals recorded at the surface may reflect the multi-fault source and result in a higher-
706 angle composite focal mechanism. Although our dynamic rupture models do not include multiple
707 faults, they appear consistent with the keystone fault model. Future dynamic rupture and seismi-
708 cycle modeling of multi-fault detachment systems could test whether dynamic stress effects may
709 allow the keystone fault mechanism to operate at lower shear stresses, modulating interseismic
710 slip on neighboring faults but rupturing well before being stressed to critical static frictional
711 failure levels.

712 All our models assume that optimally oriented faults are close to critically stressed
713 ($R_0=0.95$), which may suggest that faults better oriented than the LANF could be activated

714 earlier in the seismic cycle than the detachment. However, our assumption is in agreement with
715 the keystone fault model which postulates that high-angle faults cannot host large earthquakes
716 but bleed off excess shear stress via microseismicity and/or creep. Importantly, multi-fault
717 dynamic rupture models could explore whether any reasonable loading conditions result in
718 LANF ruptures that do not also rupture the more steeply-dipping normal faults nearby, probing
719 the complex rupture hypothesis for the lack of LANF focal mechanisms.

720

721 **5. Conclusions**

722 Data-constrained dynamic rupture modeling of the Mai'iu fault indicates that
723 subcritically stressed detachment faults dipping $<30^\circ$ at the surface can slip in $M_w > 7.0$
724 earthquakes under Andersonian extensional stress conditions. Modeled earthquakes
725 preferentially rupture to the surface along segments dipping more steeply near the surface,
726 suggesting that the most shallowly dipping detachment segments are more likely to host buried
727 ruptures that may be complemented by updip afterslip and/or interseismic creep facilitated by
728 weak, velocity-strengthening clay-rich gouges in the shallow fault zone. At shallow depths,
729 rupture may be limited by frictionally stable gouges, gentler fault dips, and dynamic stress
730 interactions with the free surface.

731 Model 4 tested the idea that frictionally weak gouge mineralogies may limit the
732 magnitude of interseismic shear stresses and strains that accumulate around the shallowest parts
733 of these faults, with excess shear stresses being relieved by shallow interseismic creep. Another
734 process that may relieve shallow interseismic stress on detachments is creep on splay faults in
735 their hanging walls, although its relative importance is unclear as such subsidiary creep is not yet
736 geodetically well-resolved. Improved satellite geodetic capabilities of upcoming missions like
737 NISAR (e.g., Rosen et al., 2017) could start to resolve not only interseismic creep on major
738 plate-boundary faults but also more detailed patterns of interseismic deformation on and between
739 minor faults nearby. These new datasets could help constrain the relative role of splay fault creep
740 in shallow interseismic shear stress accumulation around detachment faults, which our results
741 suggest could limit shallow coseismic slip and the associated seismic hazard of these faults.

742

743

744

745

746 Acknowledgments

747 Funding for this work was provided by a Green Postdoctoral Scholarship at the Institute for
748 Geophysics and Planetary Physics at Scripps Institution of Oceanography. The authors
749 acknowledge additional funding from the European Union's Horizon 2020 research and
750 innovation programme (TEAR ERC Starting grant no. 852992; ChEESE project, grant
751 agreement No. 823844), the German Research Foundation (DFG) (projects GA 2465/2-1, GA
752 2465/3-1), by KAUST-CRG (FRAGEN, grant no. ORS-2017-CRG6 3389.02) and by
753 KONWIHR – the Bavarian Competence Network for Technical and Scientific High Performance
754 Computing (project NewWave). Computing resources were provided by the Institute of
755 Geophysics of LMU Munich (Oeser et al., 2006) and the Leibniz Supercomputing Centre (LRZ,
756 project no. pr63qo). SeisSol simulations were performed on SuperMUC-NG at Leibniz-
757 Rechenzentrum (LRZ) in Munich. We thank Carsten Uphoff and Amrit Bal for their help with
758 SeisSol implementation and Samuel Webber for sharing the Mai'iu fault geometry model. We
759 acknowledge helpful discussions with Samuel Webber, Marcel Mizera, Timothy Little, Carolyn
760 Boulton, Laura Wallace, Susan Ellis, and Luc Lavier.

761

762 Open Research

763 The authors declare that all data supporting the findings of this study are available within the
764 paper and its Methods section. In particular, all data required to reproduce the earthquake models
765 can be downloaded from

766 https://drive.google.com/file/d/1v1wQvIF4rwac9GSOXDoa_I79XEME1She/view?usp=sharing

767 (which will be updated to a Zenodo repository upon revision). We use SeisSol commit tag
768 2ecef2 with branch Maiiu/f0_variable

769 (https://github.com/SeisSol/SeisSol/tree/Maiiu/f0_variable). We use projection: +proj=tmerc
770 +datum=WGS84 +k=0.9996 +lon_0=149.5376 +lat_0=-9.59178.

771

772

773

774

775

776

777

778

779 **References**

- 780 Abers, G. A., Eilon, Z., Gaherty, J. B., Jin, G., Kim, Y., Obrebski, M., & Dieck, C. (2016).
781 Southeast Papuan crustal tectonics: Imaging extension and buoyancy of an active rift.
782 *Journal of Geophysical Research: Solid Earth*, *121*(2), 951–971.
783 <https://doi.org/10.1002/2015JB012621>
- 784 Abers, G. a. (2001). Evidence for seismogenic normal faults at shallow dips in continental rifts.
785 *Geological Society, London, Special Publications*, *187*(1), 305–318.
786 <https://doi.org/10.1144/GSL.SP.2001.187.01.15>
- 787 Abers, G. A. (2009). Slip on shallow-dipping normal faults. *Geology*, *37*(8), 767–768.
788 <https://doi.org/10.1130/focus082009.1>.
- 789 Abers, G. A., Mutter, C. Z., & Fang, J. (1997). Shallow dips of normal faults during rapid
790 extension: Earthquakes in the Woodlark-D'Entrecasteaux rift system, Papua New Guinea.
791 *Journal of Geophysical Research: Solid Earth*, *102*(B7), 15301–15317.
792 <https://doi.org/10.1029/97jb00787>
- 793 Anderlini, L., Serpelloni, E., & Belardinelli, M. E. (2016). Creep and locking of a low-angle
794 normal fault: Insights from the Altotiberina fault in the Northern Apennines (Italy).
795 *Geophysical Research Letters*, *43*(9), 4321–4329. <https://doi.org/10.1002/2016GL068604>
- 796 Aochi, H. (2018). Dynamic asymmetry of normal and reverse faults due to constrained depth-
797 dependent stress accumulation. *Geophysical Journal International*, *215*(3), 2134–2143.
798 <https://doi.org/10.1093/gji/ggy407>
- 799 Aochi, H., & Madariaga, R. (2003). The 1999 İzmit, Turkey, Earthquake: Nonplanar Fault
800 Structure, Dynamic Rupture Process, and Strong Ground Motion. *Bulletin of the*
801 *Seismological Society of America*, *93*(3), 1249–1266. <https://doi.org/10.1785/0120020167>
- 802 Aochi, H., & Twardzik, C. (2020). Imaging of Seismogenic Asperities of the 2016 ML 6.0
803 Amatrice, Central Italy, Earthquake Through Dynamic Rupture Simulations. *Pure and*
804 *Applied Geophysics*, *177*(5), 1931–1946. <https://doi.org/10.1007/s00024-019-02199-z>
- 805 Aochi, H., & Ulrich, T. (2015). A probable earthquake scenario near Istanbul determined from
806 dynamic simulations. *Bulletin of the Seismological Society of America*, *105*(3), 1468–1475.
807 <https://doi.org/10.1785/0120140283>
- 808 Axen, G. J. (1992). Pore pressure, stress increase, and fault weakening in low-angle normal
809 faulting. *Journal of Geophysical Research*, *97*(B6), 8979–8991.
- 810 Axen, G. J. (2020). How a strong low-angle normal fault formed: The Whipple detachment,
811 southeastern California. *Bulletin of the Geological Society of America*, *132*(9–10), 1817–
812 1828. <https://doi.org/10.1130/B35386.1>

- 813 Axen, G. J. (2004). Mechanics of Low-Angle Normal Faults. In *Rheology and Deformation of*
814 *the Lithosphere at Continental Margins*. Columbia University Press.
815 <https://doi.org/10.7312/karn12738-004>
- 816 Biemiller, J., Taylor, F., Lavier, L., Yu, T.-L., Wallace, L., & Shen, C.-C. (2020). Emerged Coral
817 Reefs Record Holocene Low-Angle Normal Fault Earthquakes. *Geophysical Research*
818 *Letters*, 47(20). <https://doi.org/10.1029/2020GL089301>
- 819 Biemiller, J., Boulton, C., Wallace, L., Ellis, S., Little, T., Mizera, M., ... Lavier, L. (2020).
820 Mechanical Implications of Creep and Partial Coupling on the World's Fastest Slipping
821 Low-Angle Normal Fault in Southeastern Papua New Guinea. *Journal of Geophysical*
822 *Research: Solid Earth*, 125(10), 1–24. <https://doi.org/10.1029/2020JB020117>
- 823 Buck, W. R. (1988). Flexural Rotation of Normal Faults. *Tectonics*, 7(5), 959–973.
- 824 Buck, W. R. (1993). Effect of lithospheric thickness on the formation of high- and low-angle
825 normal faults. *Geology*, 21(10), 933–936. [https://doi.org/10.1130/0091-](https://doi.org/10.1130/0091-7613(1993)021<0933:EOLTOT>2.3.CO;2)
826 [7613\(1993\)021<0933:EOLTOT>2.3.CO;2](https://doi.org/10.1130/0091-7613(1993)021<0933:EOLTOT>2.3.CO;2)
- 827 Cheloni, D., De Novellis, V., Albano, M., Antonioli, A., Anzidei, M., Atzori, S., ... Doglioni, C.
828 (2017). Geodetic model of the 2016 Central Italy earthquake sequence inferred from InSAR
829 and GPS data. *Geophysical Research Letters*, 44(13), 6778–6787.
830 <https://doi.org/10.1002/2017GL073580>
- 831 Collettini, C. (2011). The mechanical paradox of low-angle normal faults: Current understanding
832 and open questions. *Tectonophysics*, 510(3–4), 253–268.
833 <https://doi.org/10.1016/j.tecto.2011.07.015>
- 834 Collettini, C., & Sibson, R. H. (2001). Normal faults, normal friction? *Geology*, 29(10), 927.
835 [https://doi.org/10.1130/0091-7613\(2001\)029<0927:NFNF>2.0.CO;2](https://doi.org/10.1130/0091-7613(2001)029<0927:NFNF>2.0.CO;2)
- 836 Di Toro, G., Han, R., Hirose, T., De Paola, N., Nielsen, S., Mizoguchi, K., ... Shimamoto, T.
837 (2011). Fault lubrication during earthquakes. *Nature*, 471(7339), 494–499.
838 <https://doi.org/10.1038/nature09838>
- 839 Douilly, R., Aochi, H., Calais, E., & Freed, A. M. (2015). Three-dimensional dynamic rupture
840 simulations across interacting faults: The Mw7.0, 2010, Haiti earthquake. *Journal of*
841 *Geophysical Research: Solid Earth*, 120(2), 1108–1128.
842 <https://doi.org/10.1002/2014JB011595>
- 843 Dunham, E. M., Belanger, D., Cong, L., & Kozdon, J. E. (2011). Earthquake ruptures with
844 strongly rate-weakening friction and off-fault plasticity, part 1: Planar faults. *Bulletin of the*
845 *Seismological Society of America*, 101(5), 2296–2307. <https://doi.org/10.1785/0120100075>

- 846 Eilon, Z., Abers, G. A., Gaherty, J. B., & Jin, G. (2015). Imaging continental breakup using
847 teleseismic body waves: The Woodlark Rift, Papua New Guinea. *Geochemistry,*
848 *Geophysics, Geosystems, 16*(8), 2529–2548. <https://doi.org/10.1002/2015GC005835>
- 849 Fletcher, J. M., Oskin, M. E., & Teran, O. J. (2016). The role of a keystone fault in triggering the
850 complex El Mayor-Cucapah earthquake rupture. *Nature Geoscience, 9*(4), 303–307.
851 <https://doi.org/10.1038/ngeo2660>
- 852 Fletcher, J. M., Teran, O. J., Rockwell, T. K., Oskin, M. E., Hudnut, K. W., Mueller, K. J., ...
853 González-García, J. (2014). Assembly of a large earthquake from a complex fault system:
854 Surface rupture kinematics of the 4 April 2010 El Mayor-Cucapah (Mexico) Mw 7.2
855 earthquake. *Geosphere, 10*(4), 797–827. <https://doi.org/10.1130/GES00933.1>
- 856 Gabriel, A. A., Ampuero, J. P., Dalguer, L. A., & Mai, P. M. (2012). The transition of dynamic
857 rupture styles in elastic media under velocity-weakening friction. *Journal of Geophysical*
858 *Research: Solid Earth, 117*(9), 1–20. <https://doi.org/10.1029/2012JB009468>
- 859 Gallovič, F., Valentová, Ampuero, J. P., & Gabriel, A. A. (2019). Bayesian Dynamic Finite-
860 Fault Inversion: 2. Application to the 2016 Mw 6.2 Amatrice, Italy, Earthquake. *Journal of*
861 *Geophysical Research: Solid Earth, 124*(7), 6970–6988.
862 <https://doi.org/10.1029/2019JB017512>
- 863 Harris, R. A., Barall, M., Lockner, D. A., Moore, D. E., Ponce, D. A., Graymer, R. W., ...
864 Eberhart-Phillips, D. (2021). A Geology and Geodesy Based Model of Dynamic Earthquake
865 Rupture on the Rodgers Creek-Hayward-Calaveras Fault System, California. *Journal of*
866 *Geophysical Research: Solid Earth, 126*(3), 1–28. <https://doi.org/10.1029/2020JB020577>
- 867 Harris, R. A., Aagaard, B., Barall, M., Ma, S., Roten, D., Olsen, K., ... Dalguer, L. (2018). A
868 suite of exercises for verifying dynamic earthquake rupture codes. *Seismological Research*
869 *Letters, 89*(3), 1146–1162. <https://doi.org/10.1785/0220170222>
- 870 Hayman, N. W., Knott, J. R., Cowan, D. S., Nemser, E., & Sarna-Wojcicki, A. M. (2003).
871 Quaternary low-angle slip on detachment faults in Death Valley, California. *Geology, 31*(4),
872 343–346. [https://doi.org/10.1130/0091-7613\(2003\)031<0343:QLASOD>2.0.CO;2](https://doi.org/10.1130/0091-7613(2003)031<0343:QLASOD>2.0.CO;2)
- 873 Heinecke, A., Breuer, A., Rettenberger, S., Bader, M., Gabriel, A. A., Pelties, C., ... Dubey, P.
874 (2014). Petascale High Order Dynamic Rupture Earthquake Simulations on Heterogeneous
875 Supercomputers. *International Conference for High Performance Computing, Networking,*
876 *Storage and Analysis, SC, 2015-January*(January), 3–14. <https://doi.org/10.1109/SC.2014.6>
- 877 Kaneko, Y., & Lapusta, N. (2010). Supershear transition due to a free surface in 3-D simulations
878 of spontaneous dynamic rupture on vertical strike-slip faults. *Tectonophysics, 493*(3–4),
879 272–284. <https://doi.org/10.1016/J.TECTO.2010.06.015>

- 880 Kaneko, Y., Avouac, J. P., & Lapusta, N. (2010). Towards inferring earthquake patterns from
881 geodetic observations of interseismic coupling. *Nature Geoscience*, 3(5), 363–369.
882 <https://doi.org/10.1038/ngeo843>
- 883 Kyriakopoulos, C., Oglesby, D. D., Funning, G. J., & Ryan, K. J. (2017). Dynamic Rupture
884 Modeling of the M7.2 2010 El Mayor-Cucapah Earthquake: Comparison With a Geodetic
885 Model. *Journal of Geophysical Research: Solid Earth*, 122(12), 10,263–10,279.
886 <https://doi.org/10.1002/2017JB014294>
- 887 Lavier, L. L., Buck, W. R., & Poliakov, A. (1999). Self-consistent rolling-hinge model for the
888 evolution of large-onset low-angle normal faults. *Geology*, 27(12), 1127–1130.
889 [https://doi.org/10.1130/0091-7613\(1999\)027<1127:SCRHMF>2.3.CO;2](https://doi.org/10.1130/0091-7613(1999)027<1127:SCRHMF>2.3.CO;2)
- 890 Lavier, L. L., Buck, W. R., & Poliakov, A. N. B. (2000). Factors controlling normal fault offset
891 in an ideal brittle layer. *Journal of Geophysical Research: Solid Earth*, 105(B10), 23431–
892 23442. <https://doi.org/10.1029/2000JB900108>
- 893 Lin, W., Byrne, T. B., Kinoshita, M., McNeill, L. C., Chang, C., Lewis, J. C., ... Kanamatsu, T.
894 (2016). Distribution of stress state in the Nankai subduction zone, southwest Japan and a
895 comparison with Japan Trench. *Tectonophysics*, 692, 120–130.
896 <https://doi.org/10.1016/j.tecto.2015.05.008>
- 897 Little, T. A., Webber, S. M., Mizera, M., Boulton, C., Oesterle, J., Ellis, S., ... Wallace, L.
898 (2019). Evolution of a rapidly slipping, active low-angle normal fault, Suckling-Dayman
899 metamorphic core complex, SE Papua New Guinea. *GSA Bulletin*.
900 <https://doi.org/10.1130/B35051.1>
- 901 Liu, Y., & Rice, J. R. (2007). Spontaneous and triggered aseismic deformation transients in a
902 subduction fault model. *Journal of Geophysical Research: Solid Earth*, 112(9).
903 <https://doi.org/10.1029/2007JB004930>
- 904 Ma, S., & Beroza, G. C. (2008). Rupture dynamics on a bimaterial interface for dipping faults.
905 *Bulletin of the Seismological Society of America*, 98(4), 1642–1658.
906 <https://doi.org/10.1785/0120070201>
- 907 Mann, P., Horton, B. K., Taylor, F. W., Shen, C., Lin, K., Renema, W., ... Renema, W. (2009).
908 Uplift patterns of reef terraces and sedimentary rocks constrain tectonic models for
909 metamorphic core complexes in eastern Papua New Guinea. *AGUFM, 2009*, G33B-0642.
- 910 Mann, P., & Taylor, F. W. (2002). Emergent Late Quaternary Coral Reefs of Eastern Papua New
911 Guinea Constrain the Regional Pattern of Oceanic Ridge Propagation. *AGUFM, 2002*,
912 T52C-1206.
- 913 Mann, P., Taylor, F. W., Gahagan, L., Watson, L., Mann, P., Taylor, F. W., ... Watson, L.
914 (2004). Rapid Kinematic and Tectonic Variations Along the 1400-km-long Australia-

- 915 Woodlark Plate Boundary Zone, Papua New Guinea and Woodlark Basin. *AGUFM*, 2004,
916 T41C-1209.
- 917 McNamara, D. D., Behboudi, E., Wallace, L., Saffer, D., Cook, A. E., Fagereng, A., ...
918 Petronotis, K. E. (2021). Variable In Situ Stress Orientations Across the Northern Hikurangi
919 Subduction Margin. *Geophysical Research Letters*, 48(5), 1–11.
920 <https://doi.org/10.1029/2020GL091707>
- 921 Melosh, H. J. (1990). Mechanical basis for low-angle normal faulting in the Basin and Range
922 province. *Nature* 1990 343:6256, 343(6256), 331–335. <https://doi.org/10.1038/343331a0>
- 923 Mizera, M., Little, T. A., Biemiller, J., Ellis, S., Webber, S., & Norton, K. P. (2019). Structural
924 and Geomorphic Evidence for Rolling-Hinge Style Deformation of an Active Continental
925 Low-Angle Normal Fault, SE Papua New Guinea. *Tectonics*, 2018TC005167.
926 <https://doi.org/10.1029/2018TC005167>
- 927 Mizera, M., Little, T., Boulton, C., Katzir, Y., Thiagarajan, N., Prior, D. J., ... Smith, E. G. C.
928 (2021). Using Syntectonic Calcite Veins to Reconstruct the Strength Evolution of an Active
929 Low-Angle Normal Fault, Woodlark Rift, SE Papua New Guinea. *Journal of Geophysical
930 Research: Solid Earth*, 126(8). <https://doi.org/10.1029/2021JB021916>
- 931 Mizera, M., Little, T., Boulton, C., Prior, D. J., Watson, E. J., Biemiller, J. B., ... Shigematsu, N.
932 (2020). Slow-to-Fast Deformation in Mafic Fault Rocks on an Active Low-Angle Normal
933 Fault, Woodlark Rift, SE Papua New Guinea. *Geochemistry, Geophysics, Geosystems*.
934 <https://doi.org/10.1002/ESSOAR.10503063.1>
- 935 Nielsen, S. B. (1998). Free surface effects on the propagation of dynamic rupture. *Geophysical
936 Research Letters*, 25(1), 125–128. <https://doi.org/10.1029/97GL03445>
- 937 Niemeijer, A. R., & Collettini, C. (2014). Frictional Properties of a Low-Angle Normal Fault
938 Under In Situ Conditions: Thermally-Activated Velocity Weakening. *Pure and Applied
939 Geophysics*, 171(10), 2641–2664. <https://doi.org/10.1007/s00024-013-0759-6>
- 940 Noda, H., Dunham, E. M., & Rice, J. R. (2009). Earthquake ruptures with thermal weakening
941 and the operation of major faults at low overall stress levels. *Journal of Geophysical
942 Research: Solid Earth*, 114(7), 1–27. <https://doi.org/10.1029/2008JB006143>
- 943 Numelin, T., Marone, C., & Kirby, E. (2007). Frictional properties of natural fault gouge from a
944 low-angle normal fault, Panamint Valley, California. *Tectonics*, 26(2), n/a-n/a.
945 <https://doi.org/10.1029/2005TC001916>
- 946 Numelin, T., Kirby, E., Walker, J. D., & Didericksen, B. (2007). Late Pleistocene slip on a low-
947 angle normal fault, Searles Valley, California. *Geosphere*, 3(3), 163–176.
948 <https://doi.org/10.1130/GES00052.1>

- 949 Oeser, J., Bunge, H.-P. & Mohr, M. Cluster design in the Earth sciences: Tethys. In *International*
950 *conference on high performance computing and communications*, 31–40 (Springer, 2006).
- 951 Oglesby, D. D., Archuleta, R. J., & Nielsen, S. B. (2000). The three-dimensional dynamics of
952 dipping faults. *Bulletin of the Seismological Society of America*, 90(3), 616–628.
953 <https://doi.org/10.1785/0119990113>
- 954 Oglesby, D. D., Archuleta, R. J., & Nielsen, S. B. (1998). Earthquakes on dipping faults: The
955 effects of broken symmetry. *Science*, 280(5366), 1055–1059.
956 <https://doi.org/10.1126/science.280.5366.1055>
- 957 Oglesby, D. D., Mai, P. M., Atakan, K., & Pucci, S. (2008). Dynamic models of earthquakes on
958 the North Anatolian fault zone under the Sea of Marmara: Effect of hypocenter location.
959 *Geophysical Research Letters*, 35(18), 2–5. <https://doi.org/10.1029/2008GL035037>
- 960 Olsen, K. B., Madariaga, R., & Archuleta, R. J. (1997). Three-dimensional dynamic simulation
961 of the 1992 Landers earthquake. *Science*, 278(5339), 834–838.
962 [https://doi.org/10.1126/SCIENCE.278.5339.834/ASSET/2DF981DB-6DC5-4BD4-9BB5-
963 1299319BEC6F/ASSETS/GRAPHIC/SE4475917005.JPEG](https://doi.org/10.1126/SCIENCE.278.5339.834/ASSET/2DF981DB-6DC5-4BD4-9BB5-1299319BEC6F/ASSETS/GRAPHIC/SE4475917005.JPEG)
- 964 Palgunadi, K. H., Gabriel, A. A., Ulrich, T., López-Comino, J. Á., & Mai, P. M. (2020).
965 Dynamic fault interaction during a fluid-injection-induced earthquake: The 2017 mw 5.5
966 pohang event. *Bulletin of the Seismological Society of America*, 110(5), 2328–2349.
967 <https://doi.org/10.1785/0120200106>
- 968 Pelties, C., Gabriel, A. A., & Ampuero, J. P. (2014). Verification of an ADER-DG method for
969 complex dynamic rupture problems. *Geoscientific Model Development*, 7(3), 847–866.
970 <https://doi.org/10.5194/gmd-7-847-2014>
- 971 Perez-Silva, A., Li, D., Gabriel, A. A., & Kaneko, Y. (2021). 3D Modeling of Long-Term Slow
972 Slip Events Along the Flat-Slab Segment in the Guerrero Seismic Gap, Mexico.
973 *Geophysical Research Letters*, 48(13), e2021GL092968.
974 <https://doi.org/10.1029/2021GL092968>
- 975 Ramos, M. D., Huang, Y., Ulrich, T., Li, D., Gabriel, A. A., & Thomas, A. M. (2021). Assessing
976 Margin-Wide Rupture Behaviors Along the Cascadia Megathrust With 3-D Dynamic
977 Rupture Simulations. *Journal of Geophysical Research: Solid Earth*, 126(7), 1–22.
978 <https://doi.org/10.1029/2021JB022005>
- 979 Rettenberger, S., Meister, O., Bader, M., & Gabriely, A. A. (2016). ASAGI - A parallel server
980 for adaptive geoinformation. *ACM International Conference Proceeding Series*.
981 <https://doi.org/10.1145/2938615.2938618>
- 982 Rice, J. R. (1992). Chapter 20 Fault Stress States, Pore Pressure Distributions, and the Weakness
983 of the San Andreas Fault. *International Geophysics*, 51(C), 475–503.
984 [https://doi.org/10.1016/S0074-6142\(08\)62835-1](https://doi.org/10.1016/S0074-6142(08)62835-1)

- 985 Rosen, P. A., Kim, Y., Kumar, R., Misra, T., Bhan, R., & Sagi, V. R. (2017). Global persistent
986 SAR sampling with the NASA-ISRO SAR (NISAR) mission. *2017 IEEE Radar*
987 *Conference, RadarConf 2017*, 0410–0414. <https://doi.org/10.1109/RADAR.2017.7944237>
- 988 Shi, Z., & Day, S. M. (2013). Rupture dynamics and ground motion from 3-D rough-fault
989 simulations. *Journal of Geophysical Research: Solid Earth*, *118*(3), 1122–1141.
990 <https://doi.org/10.1002/jgrb.50094>
- 991 Sibson, R. H. (1990). Rupture nucleation on unfavorably oriented faults. *Bulletin of the*
992 *Seismological Society of America*, *80*(6A), 1580–1604.
993 <https://doi.org/10.1785/BSSA08006A1580>
- 994 Skarbek, R. M., & Saffer, D. M. (2009). Pore pressure development beneath the décollement at
995 the Nankai subduction zone: Implications for plate boundary fault strength and sediment
996 dewatering. *Journal of Geophysical Research: Solid Earth*, *114*(B7), 7401.
997 <https://doi.org/10.1029/2008JB006205>
- 998 Smith, S. A. F., & Faulkner, D. R. (2010). Laboratory measurements of the frictional properties
999 of the Zuccale low-angle normal fault, Elba Island, Italy. *Journal of Geophysical Research*,
1000 *115*(B2), B02407. <https://doi.org/10.1029/2008JB006274>
- 1001 Spencer, J. E., & Chase, C. G. (1989). Role of crustal flexure in initiation of low-angle normal
1002 faults and implications for structural evolution of the basin and range province. *Journal of*
1003 *Geophysical Research: Solid Earth*, *94*(B2), 1765–1775.
1004 <https://doi.org/10.1029/JB094IB02P01765>
- 1005 Steffen, R., & Steffen, H. (2021). Reactivation of Non-Optimally Orientated Faults Due to
1006 Glacially Induced Stresses. *Tectonics*, *40*(11). <https://doi.org/10.1029/2021tc006853>
- 1007 Stein, R. S., Ergo, S., Barrientos, E., & Richter, C. F. (1985). Planar high-angle faulting in the
1008 basin and range: Geodetic analysis of the 1983 Borah Peak, Idaho, earthquake. *Journal of*
1009 *Geophysical Research: Solid Earth*, *90*(B13), 11355–11366.
1010 <https://doi.org/10.1029/JB090IB13P11355>
- 1011 Tinti, E., Casarotti, E., Ulrich, T., Taufiqurrahman, T., Li, D., & Gabriel, A. A. (2021).
1012 Constraining families of dynamic models using geological, geodetic and strong ground
1013 motion data: The Mw 6.5, October 30th, 2016, Norcia earthquake, Italy. *Earth and*
1014 *Planetary Science Letters*, *576*, 117237. <https://doi.org/10.1016/j.epsl.2021.117237>
- 1015 Townend, J., & Zoback, M. D. (2000). How faulting keeps the crust strong. *Geology*, *28*(5),
1016 399–402. [https://doi.org/10.1130/0091-7613\(2000\)028<0399:HFKTCS>2.3.CO;2](https://doi.org/10.1130/0091-7613(2000)028<0399:HFKTCS>2.3.CO;2)
- 1017 Ulrich, T., Gabriel, A. A., & Madden, E. H. (2019). Coupled , Physics-Based Modeling Reveals
1018 Earthquake Displacements are Critical to the 2018 Palu , Sulawesi Tsunami. *Pure and*
1019 *Applied Geophysics*, *176*, 4069–4109. <https://doi.org/10.1007/s00024-019-02290-5>

- 1020 Ulrich, T., Gabriel, A. A., Ampuero, J. P., & Xu, W. (2019). Dynamic viability of the 2016 Mw
1021 7.8 Kaikōura earthquake cascade on weak crustal faults. *Nature Communications*, *10*(1).
1022 <https://doi.org/10.1038/s41467-019-09125-w>
- 1023 Ulrich, T., Gabriel, A.-A., & Madden, E. H. (2020). Stress, rigidity and sediment strength control
1024 megathrust earthquake and tsunami dynamics. *EarthArXiv*.
- 1025 Uphoff, C., Rettenberger, S., Bader, M., Madden, E. H., Ulrich, T., Wollherr, S., & Gabriel, A.
1026 A. (2017). Extreme scale multi-physics simulations of the tsunamigenic 2004 sumatra
1027 megathrust earthquake. *Proceedings of the International Conference for High Performance*
1028 *Computing, Networking, Storage and Analysis, SC 2017*, *16*.
1029 <https://doi.org/10.1145/3126908.3126948>
- 1030 van Zelst, I., Wollherr, S., Gabriel, A. A., Madden, E. H., & van Dinther, Y. (2019). Modeling
1031 Megathrust Earthquakes Across Scales: One-way Coupling From Geodynamics and
1032 Seismic Cycles to Dynamic Rupture. *Journal of Geophysical Research: Solid Earth*,
1033 *124*(11), 11414–11446. <https://doi.org/10.1029/2019JB017539>
- 1034 Webber, S., Little, T. A., Norton, K. P., Österle, J., Mizera, M., Seward, D., & Holden, G.
1035 (2020). Progressive back-warping of a rider block atop an actively exhuming, continental
1036 low-angle normal fault. *Journal of Structural Geology*, *130*(May 2019).
1037 <https://doi.org/10.1016/j.jsg.2019.103906>
- 1038 Webber, S., Norton, K. P., Little, T. A., Wallace, L. M., & Ellis, S. (2018). How fast can low-
1039 angle normal faults slip? Insights from cosmogenic exposure dating of the active Mai'iu
1040 fault, Papua New Guinea. *Geology*, *46*(3), 227–230. <https://doi.org/10.1130/G39736.1>
- 1041 Wernicke, B. (1995). Low-angle normal faults and seismicity: A review. *Journal of Geophysical*
1042 *Research: Solid Earth*, *100*(B10), 20159–20174. <https://doi.org/10.1029/95jb01911>
- 1043 Westaway, R. (2005). Active low-angle normal faulting in the Woodlark extensional province,
1044 Papua New Guinea: A physical model. *Tectonics*, *24*(6), 1–25.
1045 <https://doi.org/10.1029/2004TC001744>
- 1046 Whitney, D. L., Teyssier, C., Rey, P., & Roger Buck, W. (2013). Continental and oceanic core
1047 complexes. *Bulletin of the Geological Society of America*, *125*(3–4), 273–298.
1048 <https://doi.org/10.1130/B30754.1>
- 1049 Wollherr, S., Gabriel, A. A., & Mai, P. M. (2019). Landers 1992 “Reloaded”: Integrative
1050 Dynamic Earthquake Rupture Modeling. *Journal of Geophysical Research: Solid Earth*,
1051 *124*(7), 6666–6702. <https://doi.org/10.1029/2018JB016355>
- 1052 Yin, A. (1989). Origin of regional, rooted low-angle normal faults: A mechanical model and its
1053 tectonic implications. *Tectonics*, *8*(3), 469–482. <https://doi.org/10.1029/TC008I003P00469>

- 1054 Yin, A. (1991). Mechanisms for the formation of Domal and Basinal Detachment Faults: A
1055 three-dimensional analysis. *Journal of Geophysical Research: Solid Earth*, 96(B9), 14577–
1056 14594. <https://doi.org/10.1029/91JB01113>
- 1057 Zoback, M. L., & Zoback, M. (2007). Lithosphere Stress and Deformation. *Treatise on*
1058 *Geophysics: Second Edition*, 6, 255–271. [https://doi.org/10.1016/B978-0-444-53802-
1059 4.00115-9](https://doi.org/10.1016/B978-0-444-53802-4.00115-9)
- 1060 Zoback, M. D., & Townend, J. (2001). Implications of hydrostatic pore pressures and high
1061 crustal strength for the deformation of intraplate lithosphere. *Tectonophysics*, 336(1–4), 19–
1062 30. [https://doi.org/10.1016/S0040-1951\(01\)00091-9](https://doi.org/10.1016/S0040-1951(01)00091-9)